

**Emittance in nonlinear Thomson scattering**Erik Johnson<sup>1,\*</sup>, Elizabeth Breen<sup>1,2</sup>, Geoffrey A. Krafft<sup>1,2</sup> and Balša Terzić<sup>1</sup><sup>1</sup>*Department of Physics, Center for Accelerator Science,  
Old Dominion University, Norfolk, Virginia 23529, USA*<sup>2</sup>*Thomas Jefferson National Accelerator Facility, Newport News, Virginia 23606, USA*

(Received 7 October 2021; accepted 7 April 2022; published 6 May 2022)

Inverse Compton scattering sources are finding increasing use as intense sources of high-energy photons. When operated at high field strength, ponderomotive detuning of the scattered emission can lead to decreased source performance. Up to now, the calculations of spectra for such nonlinear Thomson scattering have been done assuming a perfectly aligned electron interacts with the incident laser beam and several authors have investigated whether ponderomotive detuning may be mitigated or cured by suitable incident laser chirping prescriptions. In order to determine if these chirping prescriptions are suitable in real beams with nonzero emittance, it is necessary to include misaligned boundary conditions in the electron motion and calculate the resulting spectra from the exact motion. In this paper we provide the exact solution for the electron equations of motion in the case of a misaligned electron passing through a laser pulse of high field strength. This solution is then used to calculate the scattered radiation distribution and we determine the emittance limits for the simplest chirping prescription.

DOI: [10.1103/PhysRevAccelBeams.25.054401](https://doi.org/10.1103/PhysRevAccelBeams.25.054401)**I. INTRODUCTION**

Synchrotron radiation (SR) facilities generate the highest quality x-ray emissions with respect to brilliance. Through materials science, medical imaging, and fundamental physics and humanities research, nearly every aspect of modern academics benefits greatly from the research conducted with high-brilliance photon emissions. These high-end emissions, however, come at a great cost. The accelerator facilities themselves demand a great deal of power, and their construction, maintenance, and operation are quite expensive. This great expense limits the number of SR facilities in operation. Acquiring beam time is a competitive ordeal.

Inverse Compton scattering (ICS) sources provide a viable alternative to SR for much of the research being conducted at these facilities. ICS emissions are tunable, like SR. The intensity of the emissions generated via Compton scattering may be significantly less than those of SR facilities, but they are still, however, high enough for the non-destructive imaging analysis techniques commonly used by researchers. Advanced medical imaging and x-ray spectroscopy are already being conducted with Compton sources [1]. Many institutions, such as Old Dominion

University [2,3] and Technical University of Eindhoven [4], have proposed constructing their own compact ICS sources. The mobility of a high-brilliance, compact x-ray source would offer advantages that are simply not possible via SR. While not necessarily mobile, some compact ICS sources are available commercially, such as the Lyncean Compact Light Source [5]. ICS sources are already creating new research opportunities across many fields of study.

Clearly, for reliable calculations of experiment times at an inverse Compton source in the Thomson regime, it is necessary to have reliable calculations of the spectra generated by the scattering events. One approach to perform such calculations was initiated in the context of calculating undulator spectra by Coisson [6]. In this method, the undulator field is Fourier analyzed and the scattered radiation spectrum can be obtained by properly Doppler shifting the various frequency components. This same method applies in linear Thomson scattering where the incident laser electric field is Fourier analysed [2] and the scattered frequency obtained by a suitable double-Doppler shift.

Alternatively, as is done for example in the code CAIN [7], one can treat both the electron beam and photon beam as ensembles of particles and compute the scattered distribution quantum mechanically by integrating over the relevant distributions. An advantage of such an approach is that nonlinear (in the field intensity) effects on the scattered distribution can be captured in the calculation. However, as discussed in Ref. [8], because of the large number of dimensions in the integration, and the statistical way they are performed in CAIN, it may be

\*[egrim007@odu.edu](mailto:egrim007@odu.edu)

*Published by the American Physical Society under the terms of the Creative Commons Attribution 4.0 International license. Further distribution of this work must maintain attribution to the author(s) and the published article's title, journal citation, and DOI.*

difficult to obtain accurate results in some parameter regimes to quantify distribution tails without spending very large amounts of computer time.

To allow the first calculation approach to cover nonlinear Thomson scattering, the exact equations of motion of an electron in an electromagnetic plane wave were solved in the specific case of an electron antialigned with the incidence direction of the plane wave [9]. Using this approach ponderomotive spectral broadening was discovered, and later it was discovered how to correct or mitigate its deleterious effects [10,11]. However, these prescriptions were found and largely analyzed in the context of antialigned electrons (Ref. [12] is a notable exception). A main purpose of this paper is to show how more general electron orbits may be calculated exactly in an approach analogous to the method used before. This general calculation now allows the effects of beam emittance on the scattered radiation distribution to be calculated exactly. The results will be compared to an alternative calculation of nonlinear Thomson scattering published earlier in the code SENSE [8]. A main finding of our study is that for most beam conditions of relevance in real Thomson sources, the SENSE model gives very accurate results.

This paper is organized as follows. In the next section we compare two computational models designed to calculate the exact nonlinear scattered spectra: the old SENSE model developed earlier in Ref. [8] and the new, related model NLTX. Next, we compare spectra computed by SENSE and NLTX for a wide variety of beam conditions in order to document the regions of applicability of the former model. In the linear regime, we also connect the two nonlinear codes to the existing, well-documented and benchmarked linear Compton code ICCS3D [13]. Then the main results are summarized. In two Appendixes we present the exact solution for the equations of motion of an electron with arbitrary incidence angle moving into an electromagnetic plane wave, show the scattered energy distribution transforms properly under Lorentz transformation, and record equations of motion and spectra for more general scattering geometries.

## II. NONLINEAR THOMSON MODELS WITH TRANSVERSE ELECTRON MOMENTUM

Compton scattering events can be generally classified by two parameters: electron beam energy and the intensity of the incident laser pulse. Photon-electron collisions with a relatively low laser intensity, i.e., with a relatively low field strength parameter  $a_0$ , defined as the magnitude of the normalized vector potential  $eA(\xi)/m_e c$ , are described as linear while collisions with higher intensities are nonlinear. Thomson and Compton scattering events are delineated by the Compton (or recoil) parameter

$$X = \frac{4E_e E_l}{(m_e c^2)^2}. \quad (1)$$

where  $E_e$  is the mean electron and  $E_l$  mean laser beam energies,  $m_e$  is the electron mass and  $c$  the speed of light. Photon-electron collisions with relatively low electron beam energy, i.e., with a relatively low  $X$ , are called Thomson scattering events while collisions with high  $X$  are called Compton scattering events. Quasiclassical spectral calculations in the nonlinear Compton regime have been developed using the Baier-Katkov (BK) approximation [14,15] or the Wentzel-Kramers-Brillouin (WKB) model [16,17]. Quantum electrodynamic calculations have also been made in the nonlinear Compton regime [18–28]. The models presented here, however, operate in the nonlinear Thomson regime.

The calculations presented in this paper are limited to Thomson scattering events in which the expectation value of the number of emitted photons per electron is of order one or less. This condition is derived by applying collider theory to Lienard’s relativistic generalization of Larmor’s theorem [11,29]; the field strength parameter and length of the incident laser pulse need to satisfy

$$a_0^2 \sigma < \frac{3}{2\pi^{1/2} \alpha}, \quad (2)$$

where  $\sigma = cT/\lambda$  is the normalized length of the laser pulse and  $T$  is time duration of the laser pulse. This condition is well documented [30–32]. Naturally, due to the quantum stochastic nature of the scattering process, more or less photons may actually be emitted by a single electron under the limitations of Eq. (2). In addition, such a choice of parameters ensures that the electrons will not experience radiation reaction; the exact solution of the Landau-Lifshitz equation [33] in a plane wave shows  $h(\xi) - 1 \ll 1$  [34] for these parameters.

These computational models compute the scattered spectra by numerically integrating an energy density spectrum  $d^2 E'/d\omega' d\Omega$ , which is a function that defines the total scattered photon energy  $E'$  per scattered photon frequency  $\omega'$  that is scattered into a given solid angle  $d\Omega$ . This energy density spectrum is integrated over the solid angle of a sensor aperture numerically since these energy density function cannot be integrated analytically.

The energy density spectrum for both models are derived first by solving the Hamilton-Jacobi equation in order to find the equations of motion for the electron as it experiences the incident laser pulse. As a charged particle is accelerated it emits radiation, and this emitted radiation is calculated from the equations of motion to compute the energy density spectrum. Both models are computationally implemented into computer codes, SENSE and NLTX, written in Python and optimized to run in parallel. The highly oscillatory Hamilton-Jacobi integrals that arise from the equations of motion are solved numerically using deterministic Newton-Cotes rules of integration, and the integration over the solid angle is computed using Monte Carlo

integration. The two codes share a set of common features crucial in simulating realistic experiments: (1) An arbitrary electron beam distribution, including energy spread and emittance. (2) 3D model for the laser pulse. This feature is implemented by varying the effective field parameter for each electron based on its distance from the laser's center at the moment of scattering [8]:

$$a_0^{\text{eff}} = a_0 \exp[-x^2/(2\sigma_{l,x}^2) - y^2/(2\sigma_{l,y}^2)], \quad (3)$$

where  $\sigma_{l,x}$  and  $\sigma_{l,y}$  are the horizontal and vertical sizes of the laser pulse. Naturally, in the limit  $\sigma_{l,x} \rightarrow \infty, \sigma_{l,y} \rightarrow \infty$ ,  $a_0^{\text{eff}} \rightarrow a_0$ , and the 1D plane wave model is recovered. (3) An arbitrary nonlinear chirp of the laser pulse, for compensation of the narrow bandwidth [11]. (4) Finite aperture (either circular and rectangular). (5) An arbitrary shape of the laser pulse. A normalized laser pulse sampled at a discrete set of points is supplied as an input file. The details of the implementation of the first 4 features for SENSE were described in Ref. [8], while the feature 5, as well as the rectangular aperture in feature 4 are new for both codes. In what follows, we describe each model in turn, making contact between them when appropriate. In the Results section, we will show through numerical simulations that the two models—the approximate SENSE and the exact NLTX—are in near-perfect agreement.

Originally proposed by Ghebregziabher *et al.*, chirping is a method by which the frequency of the incident laser pulse is changed or modulated over its duration in order to increase brilliance in the scattered spectrum [10]. In the plane-wave approximation this frequency modulation (FM) is defined by the function  $f(\xi)$  which modifies the phase of the normalized incident laser pulse vector potential

$$\tilde{A}(\xi) = \frac{eA(\xi)}{m_e c} = a(\xi) \cos\left[\frac{2\pi\xi f(\xi)}{\lambda}\right], \quad (4)$$

where  $e$  is the electron charge,  $\xi = z + ct$  is the coordinate along the laser pulse,  $a(\xi)$  is the envelope of the vector potential, and  $\lambda$  is the wavelength of the incident photons. The optimal solution for any envelope shape in the plane-wave approximation may be found through the integral [11]

$$f_{\text{OPT}}(\xi) = \frac{1}{1 + a_0^2/2} \left( 1 + \frac{\int_0^\xi a^2(\xi') d\xi'}{2\xi} \right), \quad (5)$$

where  $a_0$  is the field strength of the vector potential. Optimized solutions have also been developed for incident laser fields outside of the plane-wave approximation [8,12]. The computational models presented in this paper can simulate any general FM function  $f(\xi)$  for both the plane-wave approximation and for a 3D laser field representation.

While the phase modulation of the optimal FM function recovers the maximum spectral brilliance from deleterious nonlinear effects, the integral in Eq. (5) may be difficult to

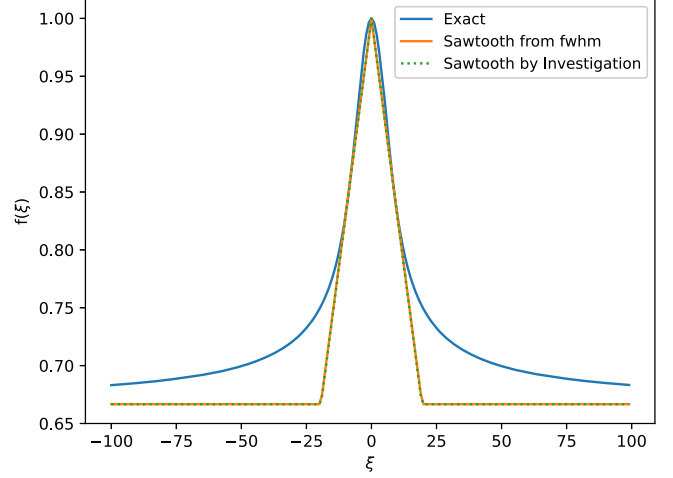


FIG. 1. FM prescription as a function of  $\xi$ . This plot compares three different FM functions: the optimal chirping solution [11], a sawtooth chirping function with a slope calculated from full width half max to peak, and the optimal sawtooth chirping function found by investigating spectral peak increase with varying slope values. The chirping prescription using slope between FWHM and the peak provides the optimal spectral peak increase.

reproduce experimentally. In this paper it will be shown that much simpler sawtooth chirping function may also be used to meaningfully improve the spectral brilliance of ICS in the nonlinear regime:

$$f_{\text{ST}}(\xi) = 1 - m|\xi|, \quad (6)$$

where  $m$  is some constant that is the slope of the function. The most effective slope of the sawtooth function  $m$  may be calculated from the optimal chirping. Figure 1 compares the optimal FM function  $f_{\text{OPT}}(\xi)$  and the sawtooth function  $f_{\text{ST}}(\xi)$ . For a Gaussian laser pulse, the most effective value for the sawtooth slope  $m$  may be found by calculating the slope of the line that passes through the peak of the of the optimal chirping function and its full-width-half-max (FWHM).

### A. SENSE model: Hamilton-Jacobi equation of motion for an on-axis electron and a coordinate transform

SENSE (simulation of emitted nonlinear scattering events) [8] is a nonlinear Thomson (non-negligible  $a_0$  and electron recoil is neglected) code that calculates scattered radiation by integrating the spectrum of a single electron colliding with an arbitrary 3D laser pulse over a distribution of electrons. It computes total scattered spectra at arbitrary angles  $\phi$  and  $\theta$  from the collision point [8]:

$$\frac{d^2 E'}{d\omega' d\Omega} = \frac{d^2 E'_\perp}{d\omega' d\Omega} + \frac{d^2 E'_\parallel}{d\omega' d\Omega}, \quad (7)$$

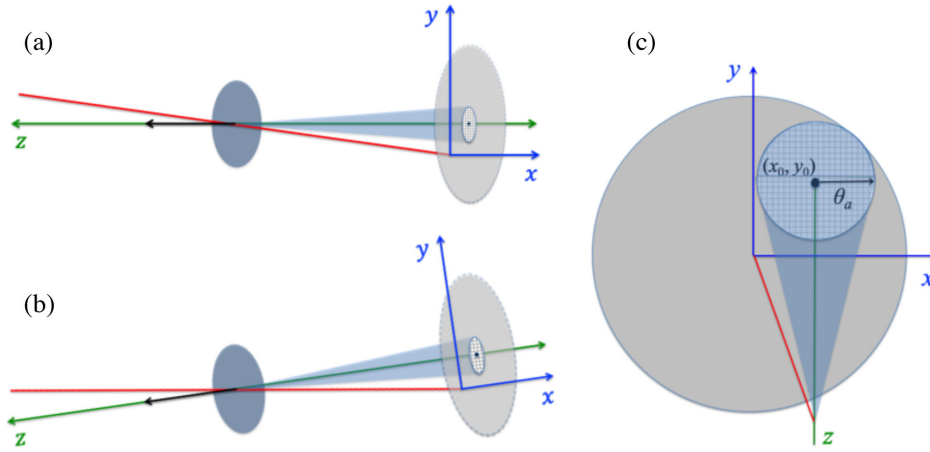


FIG. 2. Coordinate transform for SENSE code. Panel (a): Layout with the electron beam, the laser pulse (blue ellipse) and the aperture (checked oval) all along the  $z$ -axis (green line). An electron with angles  $p_x/p$  and  $p_y/p$  follows the trajectory denoted by the red line. Scattered radiation computed by SENSE and collected at the aperture (here shown as circular aperture with the maximum opening of  $\theta_a$ , but can otherwise take on different shapes) is shown as a blue cone. Large grey circle denotes the plane which contains the aperture. The angle at which an electron passes through the laser pulse is given by the intersection of red and black lines. Panel (b): SENSE transforms the problem into a coordinate system in which each electron is aligned with the  $z$ -axis. The angle by which the aperture is offset at  $(x_0, y_0)$  is given by the intersection of red and green lines. Panel (c): Head-on view of the plane of the aperture (checked circle).

where

$$\begin{aligned} \frac{d^2 E'_{\perp}}{d\omega' d\Omega} &= \frac{e^2 \omega'^2}{16\pi^3 \epsilon_0 c^3} |D_1|^2 \sin^2 \phi, \\ \frac{d^2 E'_{\parallel}}{d\omega' d\Omega} &= \frac{e^2 \omega'^2}{16\pi^3 \epsilon_0 c^3} \left| D_1 \left( \frac{\cos \theta - \beta_z}{1 - \beta_z \cos \theta} \right) \cos \phi + D_2 \sin \theta \right|^2, \\ D_{1,2} &= c_{1,2} \int_{-\infty}^{\infty} \tilde{A}^{1,2}(\xi) d\xi \exp \left[ i\omega' \left( \frac{\xi(1 - \beta_z \cos \theta)}{c(1 + \beta_z)} \right. \right. \\ &\quad \left. \left. - \frac{\sin \theta \cos \phi}{c\gamma(1 + \beta_z)} \int_{-\infty}^{\xi} \tilde{A}(\xi') d\xi' \right. \right. \\ &\quad \left. \left. + \frac{(1 + \cos \theta)}{2c\gamma^2(1 + \beta_z)^2} \int_{-\infty}^{\xi} \tilde{A}^2(\xi') d\xi' \right) \right], \end{aligned} \quad (8)$$

with  $c_1 = 1/[\gamma(1 + \beta_z)]$  and  $c_2 = 1/[\gamma^2(1 + \beta_z)(1 + \beta_z \cos \theta)]$ . The total spectrum is computed by integrating spectra over a finite physical aperture  $d\Omega$  over which the radiation is collected

$$\frac{dE}{d\omega'} = \int \frac{d^2 E}{d\omega' d\Omega} d\Omega. \quad (9)$$

These calculations are based on Ref. [9], which provides an analytic result of a ICS spectrum produced by a head-on collision of a single on-axis electron with a 1D laser plane wave. SENSE then uses a coordinate transform shown in Fig. 2 to model the emittance effects. To reiterate: modeling emittance effects is precisely the crux of the difference between the two models (and the respective codes)—SENSE uses Hamilton-Jacobi solutions for an on-axis electron paired with an appropriate coordinate transform, while

NLTX uses general Hamilton-Jacobi solutions for an electron with arbitrary angles. The former is an approximation, while the latter is exact.

## B. NLTX model: General Hamilton-Jacobi equation of motion

The nonlinear Thomson model with generalized transverse electron momentum (NLTX) has been developed in order to assess the limits of the approximation adopted by the SENSE calculation. NLTX implements a novel solution to the equations of motion for the ICS electron, so it does not rely on the parameterization of the on-axis electron spectral calculations. The fully generalized energy density spectrum is derived here.

To obtain the scattered radiation spectrum, start with the classical expressions for the far field radiation pattern [32]. The energy radiated by a moving charged particle is

$$\frac{d^2 E'}{d\omega' d\Omega} = \frac{e^2 \omega'^2}{16\pi^3 \epsilon_0 c} \left| \int_{-\infty}^{\infty} \mathbf{n} \times (\mathbf{n} \times \boldsymbol{\beta}) e^{i\omega'(t - \mathbf{n} \cdot \mathbf{r}(t)/c)} dt \right|^2, \quad (10)$$

where  $E'$  is the scattered energy,  $\omega'$  is the scattered angular frequency,  $d\Omega$  is the solid angle into which the scattering occurs, and the particle orbit is expressed as a function of time through  $\mathbf{r}(t)$ . We have denoted the scattered frequency and energy with primes to be consistent with usual field theory notation. In Appendix A, the exact solution of the equation of motion of a particle in a plane wave is given. The independent variable in the solution is  $\xi = z + ct$ , the position of the particle within the incident field of the laser. By the change of variable formula, this integral is just as well integrated as

$$\frac{d^2 E'}{d\omega' d\Omega} = \frac{e^2 \omega'^2}{16\pi^3 \epsilon_0 c^3} \left| \int_{-\infty}^{\infty} \mathbf{n} \times \left( \mathbf{n} \times \frac{d\mathbf{r}}{d\xi} \right) e^{i\omega'(t(\xi) - \mathbf{n} \cdot \mathbf{r}(\xi)/c)} d\xi \right|^2, \quad (11)$$

To get the energy into a specific polarization, the integral is performed with the vector part of Eq. (10) dotted into the polarization vector. Following the usual procedure, the polarization of the scattered radiation is resolved into components perpendicular and parallel to the plane of scattering. When the scattered radiation propagates in the

direction  $(\sin \theta \cos \phi, \sin \theta \sin \phi, \cos \theta)$ , the perpendicular direction is  $\hat{\mathbf{e}}_{\perp} = (-\sin \phi, \cos \phi, 0)$  and the parallel direction is  $\hat{\mathbf{e}}_{\parallel} = (\cos \theta \cos \phi, \cos \theta \sin \phi, -\sin \theta)$ . Because the arrival time of the scattered photon at the detector is not measured, the constant offsets in the radiation integral, which appear only in the overall phase of the scattered radiation, are unimportant.

The component of the energy density spectrum radiating with polarization perpendicular to the plane of collision is

$$\begin{aligned} \frac{d^2 E'_{\perp}}{d\omega' d\Omega} = & \frac{e^2 \omega'^2}{16\pi^3 \epsilon_0 c^3} \left| D_1 \sin \phi - \beta_x \frac{[\beta_x(1 + \cos \theta)/(1 + \beta_z) - \sin \theta \cos \phi] D_1 + (1 + \cos \theta) D_2}{1 - \beta_x \cos \phi \sin \theta - \beta_y \sin \phi \sin \theta - \beta_z \cos \theta} \sin \phi \right. \\ & \left. + \beta_y \frac{[\beta_x(1 + \cos \theta)/(1 + \beta_z) - \sin \theta \cos \phi] D_1 + (1 + \cos \theta) D_2}{1 - \beta_x \cos \phi \sin \theta - \beta_y \sin \phi \sin \theta - \beta_z \cos \theta} \cos \phi \right|^2, \end{aligned} \quad (12)$$

and the component of the energy density spectrum radiating with polarization parallel to the plane of collision is

$$\begin{aligned} \frac{d^2 E'_{\parallel}}{d\omega' d\Omega} = & \frac{e^2 \omega'^2}{16\pi^3 \epsilon_0 c^3} \left| D_1 \cos \phi \cos \theta + D_1 \sin \theta \frac{\beta_x}{1 + \beta_z} + D_2 \sin \theta \right. \\ & - \beta_x \frac{[\beta_x(1 + \cos \theta)/(1 + \beta_z) - \sin \theta \cos \phi] D_1 + (1 + \cos \theta) D_2}{1 - \beta_x \cos \phi \sin \theta - \beta_y \sin \phi \sin \theta - \beta_z \cos \theta} \cos \phi \cos \theta \\ & - \beta_y \frac{[\beta_x(1 + \cos \theta)/(1 + \beta_z) - \sin \theta \cos \phi] D_1 + (1 + \cos \theta) D_2}{1 - \beta_x \cos \phi \sin \theta - \beta_y \sin \phi \sin \theta - \beta_z \cos \theta} \sin \phi \cos \theta \\ & \left. + \beta_z \frac{[\beta_x(1 + \cos \theta)/(1 + \beta_z) - \sin \theta \cos \phi] D_1 + (1 + \cos \theta) D_2}{1 - \beta_x \cos \phi \sin \theta - \beta_y \sin \phi \sin \theta - \beta_z \cos \theta} \sin \theta \right|^2, \end{aligned} \quad (13)$$

where

$$\begin{aligned} D_1(\omega'; \theta, \varphi) &= \frac{1}{\gamma(1 + \beta_z)} \int \frac{e A_x(\xi)}{m_e c} e^{i\Phi} d\xi, \\ D_2(\omega'; \theta, \varphi) &= \frac{1}{\gamma^2(1 + \beta_z)^2} \int \frac{e^2 A_x^2(\xi)}{2m_e^2 c^2} e^{i\Phi} d\xi, \\ \Phi(\xi) &= \frac{\omega'}{c} \left( \xi \frac{(1 - \beta_x \sin \theta \cos \varphi - \beta_y \sin \theta \sin \varphi - \beta_z \cos \theta)}{1 + \beta_z} + \left[ \frac{\beta_x(1 + \cos \theta)}{\gamma(1 + \beta_z)^2} - \frac{\sin \theta \cos \varphi}{\gamma(1 + \beta_z)} \right] \int_{-\infty}^{\xi} \frac{e A_x(\xi')}{m_e c} d\xi' \right. \\ & \left. + \frac{(1 + \cos \theta)}{\gamma^2(1 + \beta_z)^2} \int_{-\infty}^{\xi} \frac{e^2 A_x^2(\xi')}{2m_e^2 c^2} d\xi' \right). \end{aligned} \quad (14)$$

During these derivations, it is important to convert nonconvergent integrals of the form  $\int e^{i\Phi} d\xi$  to convergent ones using integration by parts neglecting the boundary terms, a procedure that can be rigorously justified. For example

$$\begin{aligned}
\int e^{i\Phi} d\xi &= \frac{c}{i\omega' (1 - \beta_x \sin \theta \cos \varphi - \beta_y \sin \theta \sin \varphi - \beta_z \cos \theta)} \frac{1 + \beta_z}{1 + \beta_z} \\
&\times \int e^{i\Phi} d \left( \exp \left\{ i \frac{\omega'}{c} \left( \xi \frac{(1 - \beta_x \sin \theta \cos \varphi - \beta_y \sin \theta \sin \varphi - \beta_z \cos \theta)}{1 + \beta_z} \right) \right\} \right) \\
&\rightarrow -\frac{c}{i\omega' (1 - \beta_x \sin \theta \cos \varphi - \beta_y \sin \theta \sin \varphi - \beta_z \cos \theta)} \int i \frac{d\hat{\Phi}}{d\xi} e^{i\Phi} d\xi \\
&= -\frac{1 + \beta_z}{(1 - \beta_x \sin \theta \cos \varphi - \beta_y \sin \theta \sin \varphi - \beta_z \cos \theta)} \\
&\times \int \left\{ \left[ \frac{\beta_x(1 + \cos \theta)}{\gamma(1 + \beta_z)^2} - \frac{\sin \theta \cos \varphi}{\gamma(1 + \beta_z)} \right] \frac{eA_x(\xi)}{m_e c} + \frac{(1 + \cos \theta) e^2 A_x^2(\xi)}{\gamma^2(1 + \beta_z)^2 2m_e^2 c^2} \right\} e^{i\Phi} d\xi \\
&= -\frac{[\beta_x(1 + \cos \theta) - (1 + \beta_z) \sin \theta \cos \varphi] D_1 + (1 + \beta_z)(1 + \cos \theta) D_2}{(1 - \beta_x \sin \theta \cos \varphi - \beta_y \sin \theta \sin \varphi - \beta_z \cos \theta)} \quad (15)
\end{aligned}$$

where

$$\hat{\Phi} = \frac{\omega'}{c} \left( \left[ \frac{\beta_x(1 + \cos \theta)}{\gamma(1 + \beta_z)^2} - \frac{\sin \theta \cos \varphi}{\gamma(1 + \beta_z)} \right] \int_{-\infty}^{\xi} \frac{eA_x(\xi')}{m_e c} d\xi' + \frac{(1 + \cos \theta)}{\gamma^2(1 + \beta_z)^2} \int_{-\infty}^{\xi} \frac{e^2 A_x^2(\xi')}{2m_e^2 c^2} d\xi' \right). \quad (16)$$

The above form for the spectrum is probably easiest computationally. To facilitate later comparisons, note that the spectra can be manipulated into the form

$$\begin{aligned}
\frac{dE'_{\perp}}{d\omega' d\Omega} &= \frac{e^2 \omega'^2}{16\pi^3 \epsilon_0 c^3} \left| \frac{D_1 [\sin \varphi (1 - \beta_z \cos \theta) - \beta_y \sin \theta]}{1 - \beta_x \sin \theta \cos \varphi - \beta_y \sin \theta \sin \varphi - \beta_z \cos \theta} \right. \\
&\quad - \beta_x \frac{[\beta_x(1 + \cos \theta)/(1 + \beta_z)] D_1 + (1 + \cos \theta) D_2}{(1 - \beta_x \sin \theta \cos \varphi - \beta_y \sin \theta \sin \varphi - \beta_z \cos \theta)} \sin \varphi \\
&\quad \left. + \beta_y \frac{[\beta_x(1 + \cos \theta)/(1 + \beta_z)] D_1 + (1 + \cos \theta) D_2}{(1 - \beta_x \sin \theta \cos \varphi - \beta_y \sin \theta \sin \varphi - \beta_z \cos \theta)} \cos \varphi \right|^2 \quad (17)
\end{aligned}$$

and

$$\begin{aligned}
\frac{dE'_{\parallel}}{d\omega' d\Omega} &= \frac{e^2 \omega'^2}{16\pi^3 \epsilon_0 c^3} \left| \frac{D_1 (\cos \theta - \beta_z) \cos \varphi}{1 - \beta_x \sin \theta \cos \varphi - \beta_y \sin \theta \sin \varphi - \beta_z \cos \theta} \right. \\
&\quad - \beta_x \frac{[\beta_x(1 + \cos \theta)/(1 + \beta_z)] D_1 + (1 + \cos \theta) D_2}{1 - \beta_x \sin \theta \cos \varphi - \beta_y \sin \theta \sin \varphi - \beta_z \cos \theta} \cos \varphi \\
&\quad - \beta_y \frac{[\beta_x(1 + \cos \theta)/(1 + \beta_z)] D_1 + (1 + \cos \theta) D_2}{1 - \beta_x \sin \theta \cos \varphi - \beta_y \sin \theta \sin \varphi - \beta_z \cos \theta} \sin \varphi \\
&\quad + \frac{(1 + \beta_z) D_2}{1 - \beta_x \sin \theta \cos \varphi - \beta_y \sin \theta \sin \varphi - \beta_z \cos \theta} \sin \theta \\
&\quad \left. + \frac{\beta_x D_1}{1 - \beta_x \sin \theta \cos \varphi - \beta_y \sin \theta \sin \varphi - \beta_z \cos \theta} \sin \theta \right|^2 \quad (18)
\end{aligned}$$

by placing all the terms over a common denominator.

Finally, it is important to note that the expressions for the spectrum implicitly include that the electron charge has  $q = -e$ , where  $e$  is the (positive) proton charge. For positive particles the sign of  $D_1$  reverses but that of  $D_2$  does not. The signs of the individual terms in the spectrum

need be adjusted to accommodate as in the derivation results in the Appendixes.

### III. RESULTS

This new computational model has been used to explore the limits in which the on-axis electron approximation

adopted by SENSE remains valid. A study has been conducted to determine the efficacy of FM corrections to nonlinear effects in the case of electron beams with extremely high emittance values. NLTX simulations have also been used to gauge the merits of the sawtooth chirping function. Note that while NLTX has the capability to implement 3D modeling for the incident laser pulse, the simulation presented in this paper have been conducted within the plane-wave approximation of the incident laser pulse.

The effects of the extreme emittance are clearly evident in each set of plots. Note that for each set of plots, the normalized emittance parallel to the polarization vector, i.e., in the horizontal  $\hat{x}$  direction, increases by an order of magnitude every row. The emittance begins at  $10^{-6}$  m rad in the top row, and increases to  $10^{-5}$  and  $10^{-4}$  m rad in the middle and bottom rows respectively. Similarly, the normalized emittance perpendicular to the polarization vector, i.e., in the vertical  $\hat{y}$  direction, increases by an order of magnitude every column. The emittance begins at  $10^{-6}$  m rad in the left column, and increases to  $10^{-5}$  and  $10^{-4}$  m rad in the middle and right columns respectively. In order to observe how extreme emittance impacted the onset of nonlinear effects in scattered spectra, each set of simulations was conducted with a different value for the field strength parameter  $a_0$ . The three sets of simulations presented begin in the linear regime with  $a_0 = 0.1$ , and then the field strength is increased into the nonlinear limit with  $a_0 = 1.0$  and  $a_0 = 3.25$ .

The simulations in Fig. 3 illustrate how emittance generates spectral broadening in the linear regime: increased emittance causes the development of a spectral tail in the lower energy scattered photons. Additionally, the horizontal emittance  $\epsilon_x$  has a more severe impact on the ICS spectrum as it represents the electron motion parallel to the vector potential of the laser pulse. The onset of nonlinear effects can be seen in Fig. 4 in which  $a_0 = 1.0$ . Harmonics are beginning to emerge, and subsidiary peaks are starting to dominate the spectrum. In the top left panel of Figure 4, the burgeoning second harmonic is the small bump in the spectrum at  $\omega/\omega_0 = 1.38$ . This second harmonic scales with the normalized emittance  $\epsilon$ . This effect has been observed empirically by Kramer *et al.* [35], and SENSE has been used to replicate and analyze the scattered spectra [8]. These effects are more pronounced in Fig. 5 in which  $a_0 = 3.25$ . It is well known from undulator theory that for a linearly polarized incident laser pulse the harmonics will be red-shifted in the frequency by a factor of  $1 + a_0^2/2$ . This nonlinear redshift is evident across the three sets of simulations. For the simulations in Fig. 5, this nonlinear redshift has caused the majority of the scattered radiation to be emitted near the first harmonic. In both nonlinear sets the thermal effects smooth out

the subsidiary peaks in the scattered spectra. Observe the transformation in Fig. 5. In the top left panel the subsidiary peaks subsume the entire spectrum. As the emittance increases, the fringe interference patterns are diminished. In the bottom right panel, the subsidiary peaks are smoothed out almost entirely.

The energy density spectrum calculated using the Hamilton-Jacobi solution for electrons with generalized 3D momenta is quite different than the parametrized, on-axis approximation used by SENSE, i.e., Eq. (8) is quite different from Eqs. (12) and (13). Simulations show, however, that both expressions produce nearly identical spectra for inverse Compton scattering. Comparing the two models over a broad and extreme range of emittance values is critical to this comparison values because the primary difference between the calculations arises from the initial transverse relativistic velocity of the electron  $\beta_x, \beta_y$ . In the limit that they go to zero, the on-axis solution is recovered from the more general expression. The field strength parameter was changed to observe what role, if any, the nonlinear effects would play in the difference between these calculations. It is plainly clear from the results that even for extremely high emittance values—emittance values far beyond most operating accelerators—both models, SENSE and NLTX, produce nearly identical spectra. One may conclude that the on-axis approximation used in SENSE is valid for the backscattering collision orientation in which the crossing angle of the electron beam and the incident laser pulse is negligible.

A series of simulations were conducted to test the performance of the optimal chirping function, Eq. (5), in the case of extremely high normalized emittance. The emittance values of the simulations ranged from  $10^{-7}$  to  $10^{-4}$  m rad. The field strength parameter was fixed at unity which is firmly in the nonlinear regime. Figures 6–8 show that the exact chirping function recovers much of the spectral brilliance in the scattered spectra. In the plane-wave approximation, the optimal FM is as effective in case of extremely high emittance as it is in the on-axis electron case, i.e., when there is no emittance in the electron beam.

During this simulation study of Compton scattering with high-emittance beams, the sawtooth chirping function, Eq. (6), was also tested. Again, Figs. 6–8 show that this chirping function also recovers much of the spectral brilliance lost to nonlinear effects. In fact, this much simpler frequency modulation function performed nearly as well as Eq. (5), the optimal chirping function in the plane-wave approximation. A comparison of the maximum spectral peaks across all emittance values of the study is shown in Fig. 9. Both chirping functions produce similarly substantial gains in the peak of the scattered spectra. The successful application of the sawtooth function arose from a judicious selection of the slope

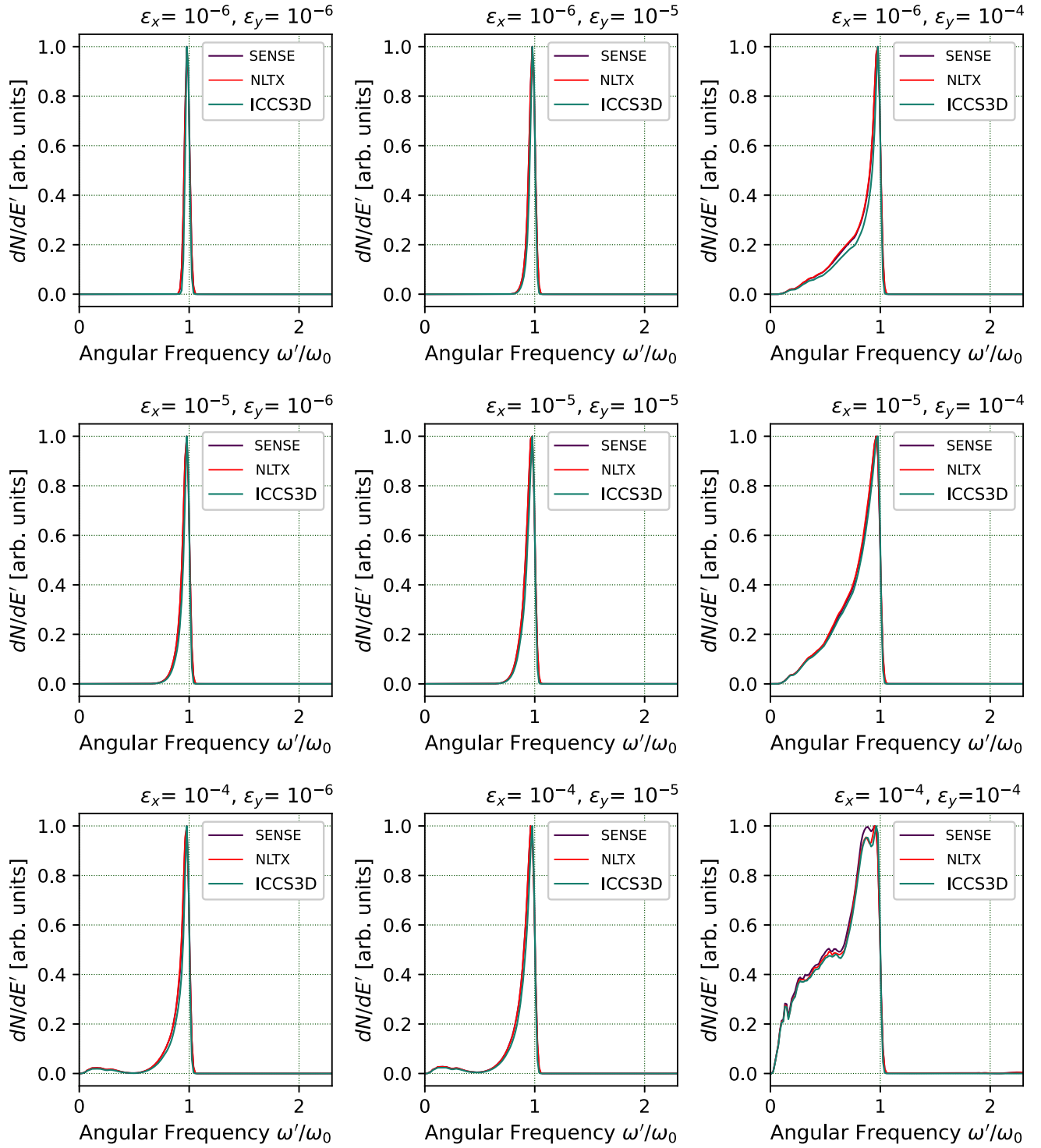


FIG. 3. Peak normalized simulated spectra from SENSE, ICCS3D, and NLTX for field strength  $a_0 = 0.1$  and a range of normalized horizontal emittance  $\epsilon_x$  and normalized vertical emittance  $\epsilon_y$  values. The following parameters were used in the simulations:  $E_e = 23$  MeV;  $\Delta E_e/E_e = 0.175\%$ ;  $\sigma_x = 41$   $\mu\text{m}$ ;  $\sigma_y = 81$   $\mu\text{m}$ ;  $\lambda = 800$  nm;  $\sigma_{x,l} = 13.59$   $\mu\text{m}$ ;  $\sigma_{y,l} = 13.59$   $\mu\text{m}$ ;  $\sigma = 5.57$ . The scattered frequency is scaled by the normalizing frequency  $\omega_0 = 2\pi c/\lambda$ .

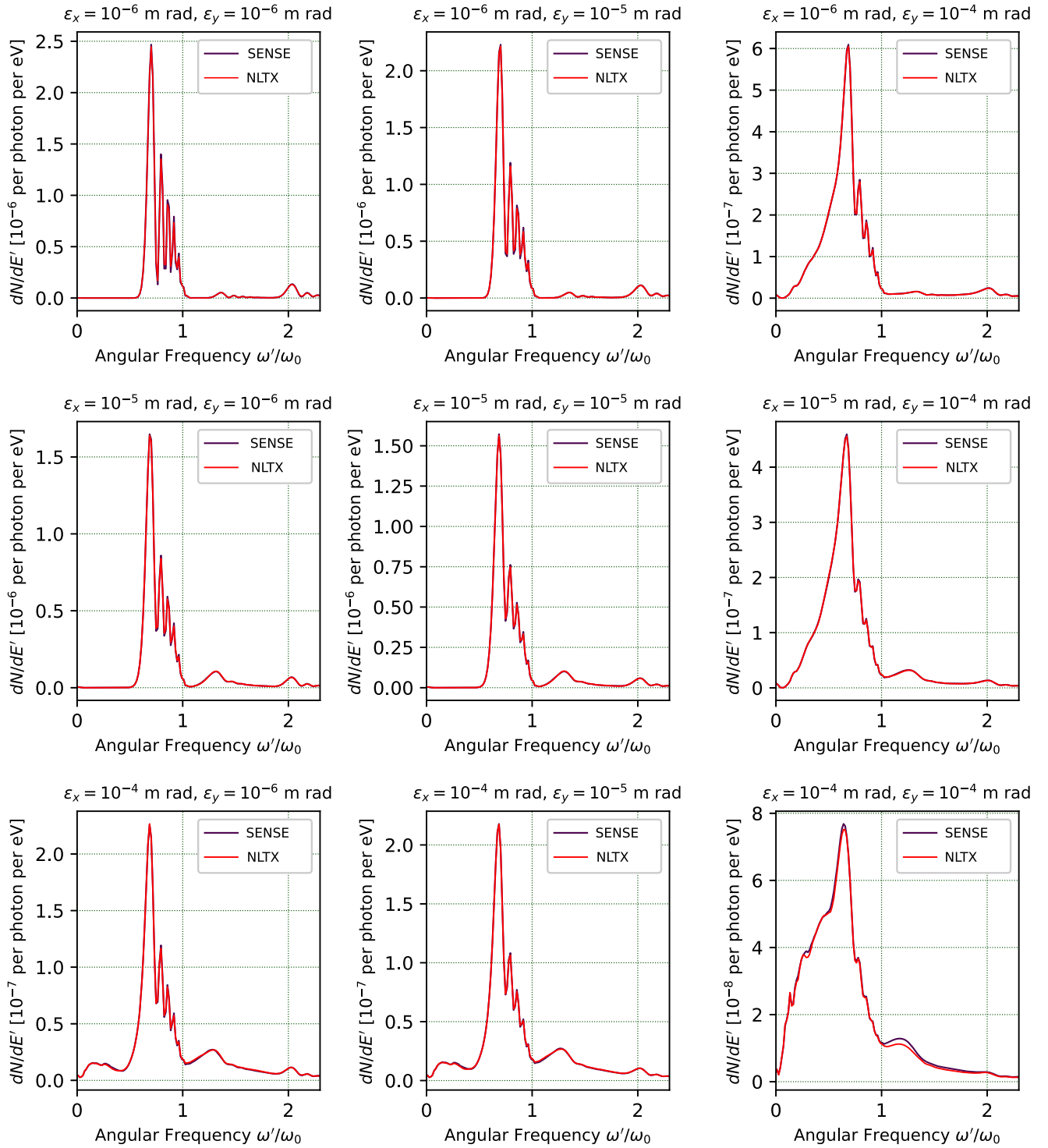


FIG. 4. Simulated spectra from SENSE and NLTX for field strength  $a_0 = 1.0$  and a range of normalized horizontal emittance  $\epsilon_x$  and normalized vertical emittance  $\epsilon_y$  values. The following parameters were used in the simulations:  $E_e = 23$  MeV;  $\Delta E_e/E_e = 0.175\%$ ,  $\sigma_x = 41$   $\mu\text{m}$ ;  $\sigma_y = 81$   $\mu\text{m}$ ;  $\lambda = 800$  nm;  $\sigma_{x,l} = 13.59$   $\mu\text{m}$ ;  $\sigma_{y,l} = 13.59$   $\mu\text{m}$ ;  $\sigma = 5.57$ . The scattered frequency is scaled by the normalizing frequency  $\omega_0 = 2\pi c/\lambda$ .

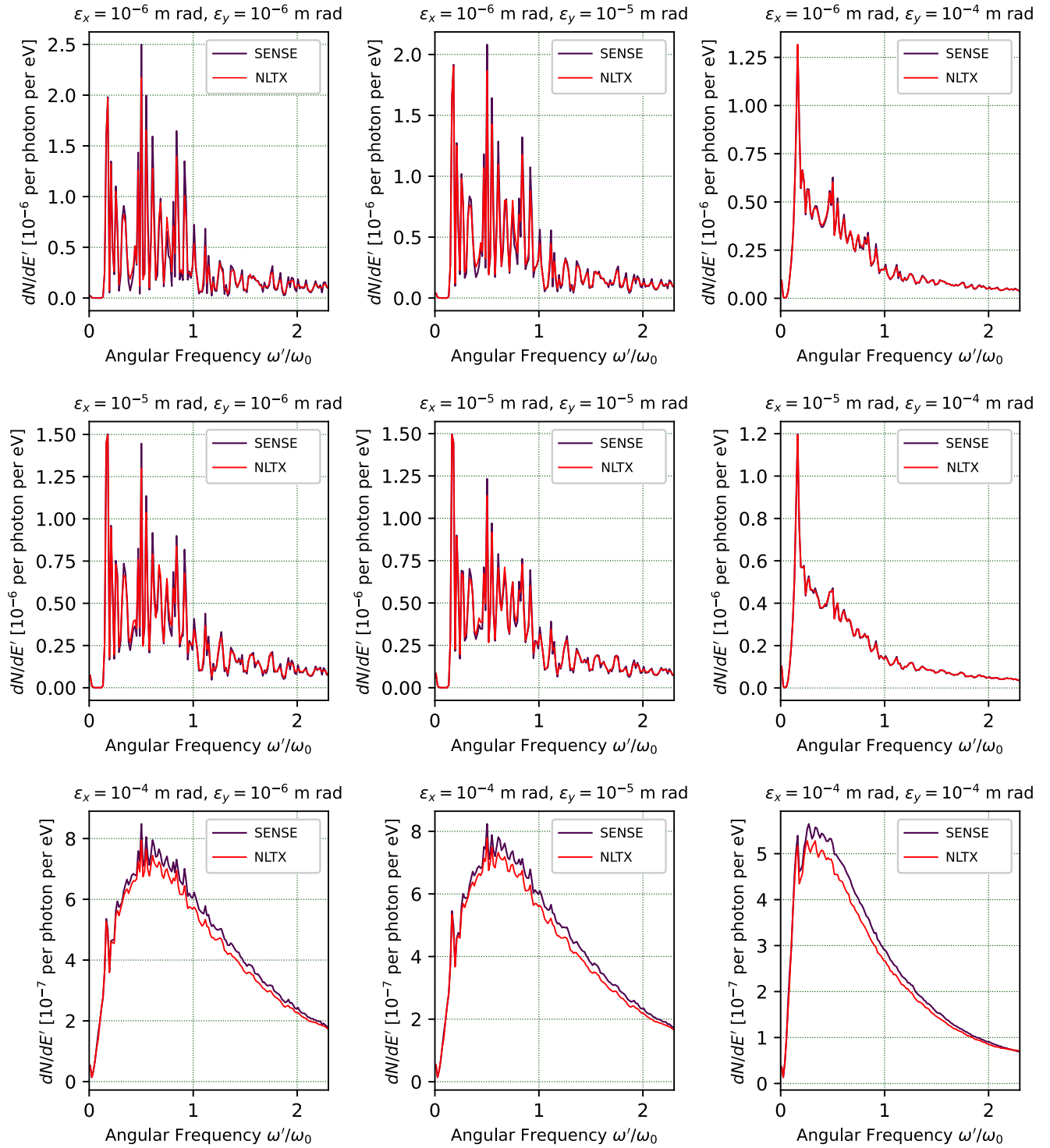


FIG. 5. Simulated spectra from SENSE and NLTX for field strength  $a_0 = 3.25$  and a range of normalized horizontal emittance  $\epsilon_x$  and normalized vertical emittance  $\epsilon_y$  values. The following parameters were used in the simulations:  $E_e = 23$  MeV;  $\Delta E_e/E_e = 0.175\%$ ;  $\sigma_x = 41$   $\mu\text{m}$ ;  $\sigma_y = 81$   $\mu\text{m}$ ;  $\lambda = 800$  nm;  $\sigma_{x,l} = 13.59$   $\mu\text{m}$ ;  $\sigma_{y,l} = 13.59$   $\mu\text{m}$ ;  $\sigma = 5.57$ . The scattered frequency is scaled by the normalizing frequency  $\omega_0 = 2\pi c/\lambda$ .

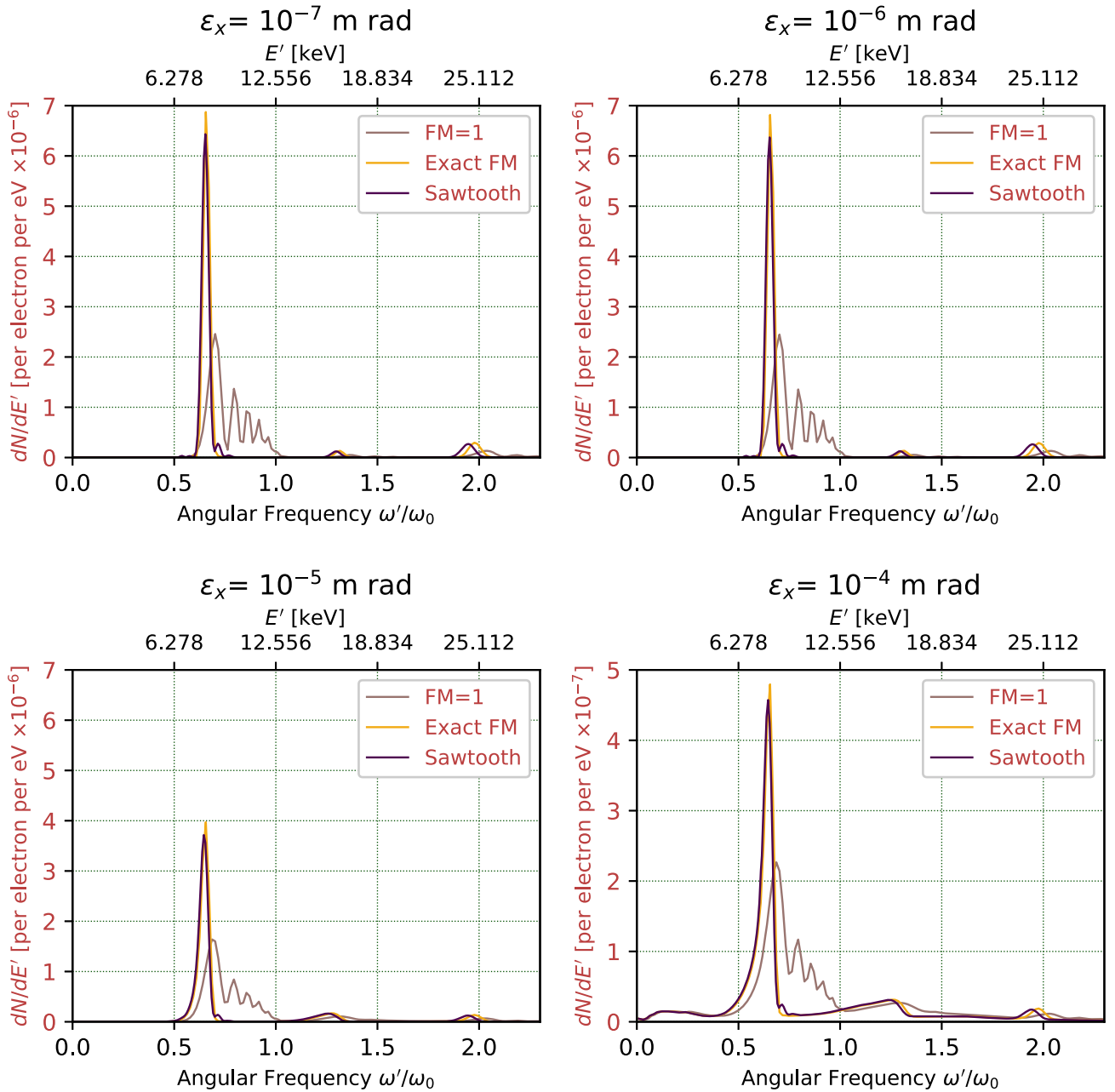


FIG. 6. Comparison of simulated spectra with three different FM functions: uncorrected simulation (FM = 1), the optimal chirping solution [11], and a sawtooth chirping function. The simulations were conducted for a range of normalized horizontal emittance  $\epsilon_x$  values. In the case of the most extreme emittance (bottom right panel), the spectra have been rescaled by an order of magnitude on the right vertical axis. The following parameters were used in the simulations:  $E_e = 23$  MeV;  $\Delta E_e/E_e = 0.175\%$ ;  $\sigma_x = 41$   $\mu\text{m}$ ;  $\sigma_y = 81$   $\mu\text{m}$ ;  $a_0 = 1.5$ ;  $\lambda = 800$  nm;  $\sigma_{x,l} = \sigma_{y,l} = 13.59$   $\mu\text{m}$ ;  $\sigma = 5.57$ . Note that the scale of the y-axis is fixed for the top two plots and the lower left plot, but the scaling on the bottom right plot has been adjusted since the peaks are a full order of magnitude smaller than the other plots.

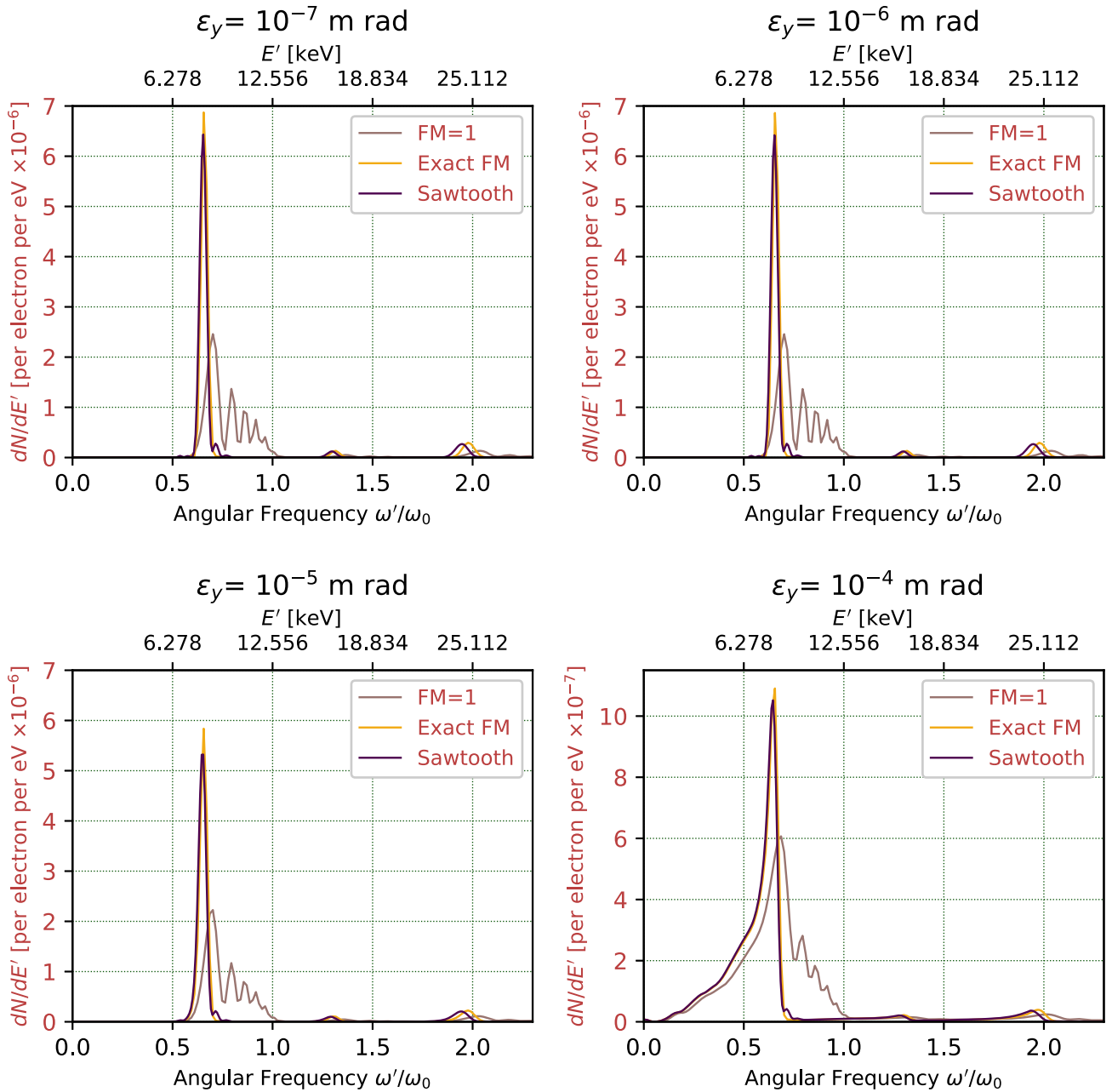


FIG. 7. Comparison of simulated spectra with three different FM functions: uncorrected simulation (FM = 1), the optimal chirping solution [11], and a sawtooth chirping function. The simulations were conducted for a range of normalized vertical emittance  $\epsilon_y$  values. In the case of the most extreme emittance (bottom right panel), the spectra have been rescaled by an order of magnitude on the right vertical axis. The following parameters were used in the simulations:  $E_e = 23$  MeV;  $\Delta E_e/E_e = 0.175\%$ ;  $\sigma_x = 41$   $\mu\text{m}$ ;  $\sigma_y = 81$   $\mu\text{m}$ ;  $a_0 = 1.5$ ;  $\lambda = 800$  nm;  $\sigma_{x,l} = \sigma_{y,l} = 13.59$   $\mu\text{m}$ ;  $\sigma = 5.57$ . Note that the scale of the y-axis is fixed for the top two plots and the lower left plot, but the scaling on the bottom right plot has been adjusted since the peaks are a full order of magnitude smaller than the other plots.

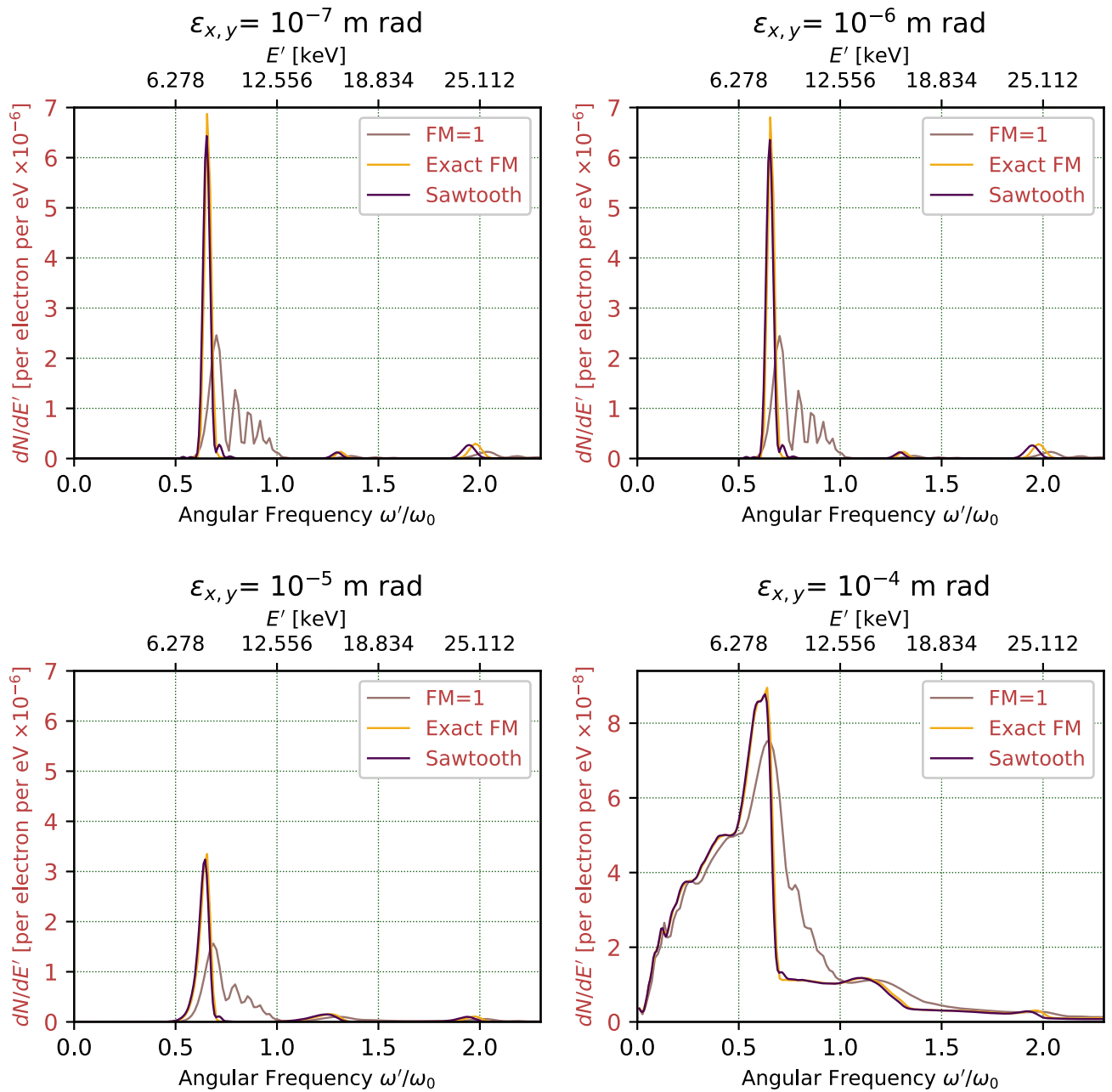


FIG. 8. Comparison of simulated spectra with three different FM functions: uncorrected simulation (FM = 1), the optimal chirping solution [11], and a sawtooth chirping function. The simulations were conducted for a range of normalized circular emittance  $\epsilon_x = \epsilon_y$  values. In the case of the most extreme emittance (bottom right panel), the spectra have been rescaled by two orders of magnitude on the right vertical axis. The following parameters were used in the simulations:  $E_e = 23$  MeV;  $\Delta E_e/E_e = 0.175\%$ ;  $\sigma_x = 41$   $\mu\text{m}$ ;  $\sigma_y = 81$   $\mu\text{m}$ ;  $a_0 = 1.5$ ;  $\lambda = 800$  nm;  $\sigma_{x,l} = \sigma_{y,l} = 13.59$   $\mu\text{m}$ ;  $\sigma = 5.57$ . Note that the scale of the y-axis is fixed for the top two plots and the lower left plot, but the scaling on the bottom right plot has been adjusted since the peaks are two orders of magnitude smaller than the other plots.

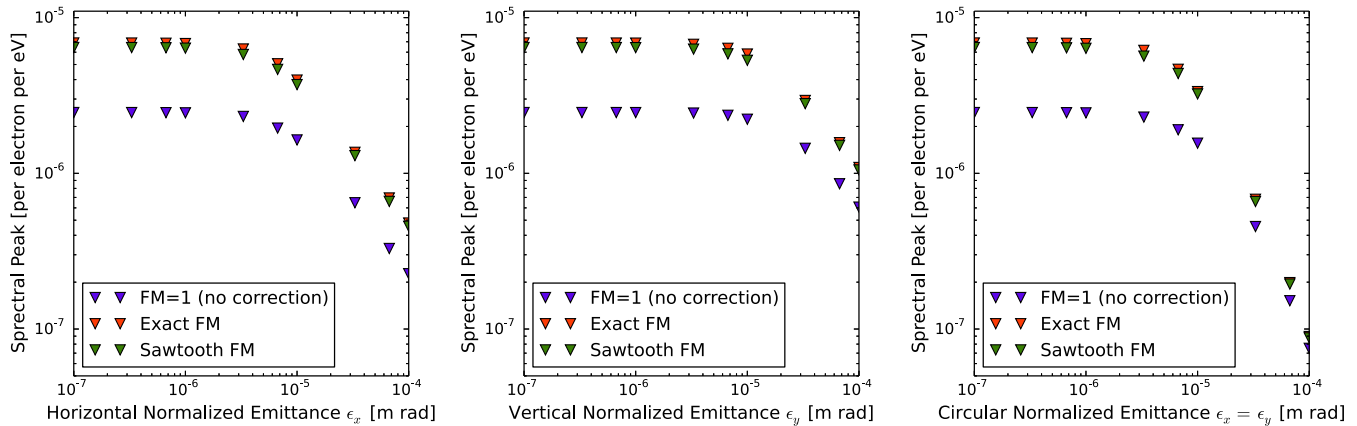


FIG. 9. Spectral peak as a function of normalized horizontal emittance (left), normalized vertical emittance (middle), and normalized circular emittance (right). These plots compare three different FM functions: uncorrected simulation (FM = 1), the optimal chirping solution [11], and a sawtooth chirping function. The following parameters were used in the simulations:  $E_e = 23$  MeV;  $\Delta E_e/E_e = 0.175\%$ ;  $\sigma_x = 41 \mu\text{m}$ ;  $\sigma_y = 81 \mu\text{m}$ ;  $a_0 = 1.5$ ;  $\lambda = 800$  nm;  $\sigma_{x,l} = \sigma_{y,l} = 13.59 \mu\text{m}$ ;  $\sigma = 5.57$ .

*m.* This constant was found by optimizing the spectral peak for the given parameters.

#### IV. CONCLUSION

A novel, broadly generalized quasiclassical calculation of inverse Compton-scattered spectra has been presented. This new spectral distribution calculation arises from solving the equations of motion for an accelerated electron with generalized 3D momenta as it experiences an incident laser pulse. The polarization vector of the incident laser also remains general in this calculation.

The new calculation has been used to develop a computational model, NLTX, to simulate ICS events. NLTX simulates an accelerated electron beam in which each individual electron is assigned its own unique generalized coordinates. Within this model a linearly polarized laser pulse with any user defined envelope shape is incident upon the electron beam in the backscattering orientation, that is the case in which the offset angle between the two is negligible. NLTX allows for the incident laser pulse to be frequency modulated, or chirped, to correct problematic nonlinear effects within the scattered spectrum.

NLTX has been used to conduct a study of the effects upon ICS spectra that arise from extreme emittance. The novelty of the new analysis stems from the more rigorous treatment of the electrons transverse momenta. Hence, the new computational model is an ideal one to study emittance. The studies presented here had two principle objectives: (1) to observe the impact of extreme emittance in the linear and nonlinear regimes and (2) to test the efficacy of FM corrections in case of electron beams with extreme emittance.

Across these simulations NLTX has been compared to two previous models, SENSE and Improved Codes for Compton Scattering (ICCS) [36]. All codes are in strong agreement in the linear regime. NLTX and SENSE are in strong

agreement in the nonlinear regime. Any approximations made in the parameterization of SENSE for the 3D envelope model did not undermine the accuracy of the generated spectrum: it is nearly exactly the same as the full transverse calculation. As SENSE has been thoroughly benchmarked, this is not a surprise for the lower emittance calculations. The agreement of the two models at absurdly high emittance values, however, is a new benchmark for the original code.

NLTX has also been used to study how extreme emittance effects spectral correction through FM, or chirping, within the plane-wave approximation. Across this study, even for cases with extreme emittance, the optimal chirping solution still restored the maximum brilliance in the corrected spectra. This maximum peak spectral density that may be recovered scales with the square of the field strength parameter  $a_0^2$ . These spectral gains are also independent of the direction of the emittance, that is, the optimal chirp function recovers spectral brilliance for vertical emittance  $\epsilon_x$ , horizontal emittance  $\epsilon_y$ , and circular emittance  $\epsilon_x = \epsilon_y$ .

The sawtooth chirping function has also been introduced during this study. Figure 6 compares the uncorrected ICS spectrum (FM = 1) to spectra corrected with the sawtooth and the optimal chirping functions for a range of horizontal emittance values  $\epsilon_x$ . In this set of simulations, both the optimal and the sawtooth corrections restore the spectral brilliance across the first three harmonics. In Figs. 7 and 8 simulations were run again with vertical emittance  $\epsilon_y$  and circular emittance  $\epsilon_x = \epsilon_y$  respectively. In all sets of simulations, the chirping functions were highly effective across all harmonics. This sawtooth function provides two substantial benefits. First, it recovers nearly as much of the spectral peak as the optimal chirping solution: about 91%–97% of the spectral peak. Second, the simple nature of the sawtooth function, as shown in Fig. 1, may make it

easier to produce experimentally than the integral in the optimal solution.

Another distinction between new, generalized calculation is that it is done in the lab frame. This new Hamilton-Jacobi solution will be necessary to simulate scattering events outside of the backscattering geometry. The time resolution required to capture the photon-electron interaction will be significantly easier to compute in the lab frame.

### ACKNOWLEDGMENTS

G. A. K. and E. B. are supported by Jefferson Science Associates, LLC under U.S. DOE Contract No. DE-AC05-06OR23177. E. B. is supported by the U.S. National Science Foundation Research Experience for Undergraduates at Old Dominion University Grant No. 1950141. E. B., E. S. J., and B. T. acknowledge the support from the U.S. National Science Foundation CAREER Grant No. 1847771.

### APPENDIX A: SOLUTION TO THE EQUATIONS OF MOTION FOR A RELATIVISTIC ELECTRON WITH TRANSVERSE MOMENTUM

In the textbook by Landau and Lifshitz [37], it is pointed out that the Hamilton-Jacobi method yields an exact solution of the motion of a charged particle in an electromagnetic plane wave. This solution applies even when the electromagnetic field strength is large enough that significant nonlinear scattering is possible. In [9], the solution is used to compute nonlinear scattered radiation spectra in the specific case that the electron is antiparallel to the incident

photon beam. In order to capture effects of emittance on the spectra, it is necessary to allow the electrons to have a spread in angles around the anti-aligned direction. In this Appendix, we solve the exact Hamilton-Jacobi motion of a relativistic particle in a plane electromagnetic wave and generalize the results of [9] to include off-axis particle motion. We also develop and utilize notations more convenient for this problem than appears in the textbook solution.

First write down the Hamilton-Jacobi solution for this problem with the more general boundary conditions. Suppose the momentum 4-vector for a relativistic electron before the arrival of the photon pulse is  $p^\mu = \gamma(1, \vec{\beta})m_e c$ , where  $\gamma$  and  $\vec{\beta}$  are the usual relativistic factors in the lab frame,  $m_e$  is the rest mass, and  $c$  is the speed of light in vacuum. The full relativistic Hamilton-Jacobi equation for the motion is

$$\left(-\frac{\partial S}{\partial t} - q\phi\right)^2 = \left(\frac{\partial S}{\partial \vec{x}} - q\vec{A}\right)^2 c^2 + m_e^2 c^4, \quad (\text{A1})$$

where  $\phi$  is the scalar potential and  $\vec{A}$  is the vector potential for the plane wave, and  $q$  is the particle charge. Assuming an  $x$ -linearly polarized incident plane wave propagating in the negative  $z$  direction, the gauge can be chosen so that  $\phi = 0$  and  $\vec{A} = A_x(ct + z)\hat{x}$ . The Hamilton-Jacobi equation should be solved with the more general boundary conditions  $\vec{\beta} \rightarrow (\beta_x, \beta_y, \beta_z)$  as  $t \rightarrow -\infty$ . An action solving the Hamilton-Jacobi equation incorporating these boundary conditions is  $S = -\sqrt{m_e^2 c^2 + \vec{p} \cdot \vec{p}} ct + \vec{p} \cdot \vec{x} + F(\xi)$  where  $\xi = ct + z$  and

$$F(\xi) = \int_{-\infty}^{\xi} \left[ \frac{p_x q A_x(\xi')}{\sqrt{m_e^2 c^2 + \vec{p} \cdot \vec{p}} + p_z} - \frac{q^2 A_x^2(\xi')/2}{\sqrt{m_e^2 c^2 + \vec{p} \cdot \vec{p}} + p_z} \right] d\xi'. \quad (\text{A2})$$

Following the method, constants of the motion are generated by taking partial derivatives of the action function with respect to the momenta. Expressing the constants in a convenient manner, the results are

$$\begin{aligned} x_0 &= \frac{\partial S}{\partial p_x} = -\frac{p_x}{\sqrt{m_e^2 c^2 + \vec{p} \cdot \vec{p}}} ct + x + \frac{1}{\sqrt{m_e^2 c^2 + \vec{p} \cdot \vec{p}} + p_z} \int_{-\infty}^{\xi} q A_x d\xi' \\ &\quad - \left[ \frac{1}{(\sqrt{m_e^2 c^2 + \vec{p} \cdot \vec{p}} + p_z)^2} \int_{-\infty}^{\xi} \left[ p_x q A_x - \frac{q^2 A_x^2}{2} \right] d\xi' \right] \frac{p_x}{\sqrt{m_e^2 c^2 + \vec{p} \cdot \vec{p}}}, \\ y_0 &= \frac{\partial S}{\partial p_y} = -\frac{p_y}{\sqrt{m_e^2 c^2 + \vec{p} \cdot \vec{p}}} ct + y - \left[ \frac{1}{(\sqrt{m_e^2 c^2 + \vec{p} \cdot \vec{p}} + p_z)^2} \int_{-\infty}^{\xi} \left[ p_x q A_x - \frac{q^2 A_x^2}{2} \right] d\xi' \right] \frac{p_y}{\sqrt{m_e^2 c^2 + \vec{p} \cdot \vec{p}}}, \\ z_0 &= \frac{\partial S}{\partial p_z} = -\frac{p_z}{\sqrt{m_e^2 c^2 + \vec{p} \cdot \vec{p}}} ct + z - \left[ \frac{1}{(\sqrt{m_e^2 c^2 + \vec{p} \cdot \vec{p}} + p_z)^2} \int_{-\infty}^{\xi} \left[ p_x q A_x - \frac{q^2 A_x^2}{2} \right] d\xi' \right] \frac{p_z + \sqrt{m_e^2 c^2 + \vec{p} \cdot \vec{p}}}{\sqrt{m_e^2 c^2 + \vec{p} \cdot \vec{p}}} \\ &= -\frac{p_z \xi}{\sqrt{m_e^2 c^2 + \vec{p} \cdot \vec{p}}} + \frac{p_z + \sqrt{m_e^2 c^2 + \vec{p} \cdot \vec{p}}}{\sqrt{m_e^2 c^2 + \vec{p} \cdot \vec{p}}} z \\ &\quad - \left[ \frac{1}{(\sqrt{m_e^2 c^2 + \vec{p} \cdot \vec{p}} + p_z)^2} \int_{-\infty}^{\xi} \left[ p_x q A_x - \frac{q^2 A_x^2}{2} \right] d\xi' \right] \frac{p_z + \sqrt{m_e^2 c^2 + \vec{p} \cdot \vec{p}}}{\sqrt{m_e^2 c^2 + \vec{p} \cdot \vec{p}}}. \end{aligned} \quad (\text{A3})$$

Manipulating these expressions, one obtains a solution of the equations of motion generalizing those in [9]

$$\begin{aligned}
ct(\xi) &= -\frac{p_0 z_0}{p_0 + p_z} - \frac{1}{(p_0 + p_z)^2} \int_{-\infty}^{\xi} \left[ p_x q A_x - \frac{q^2 A_x^2}{2} \right] d\xi' + \frac{p_0 \xi}{p_0 + p_z}, \\
x(\xi) &= x_0 - \frac{p_x z_0}{p_0 + p_z} - \frac{1}{p_0 + p_z} \int_{-\infty}^{\xi} q A_x d\xi' + \frac{p_x \xi}{p_0 + p_z}, \\
y(\xi) &= y_0 - \frac{p_y z_0}{p_0 + p_z} + \frac{p_y \xi}{p_0 + p_z}, \\
z(\xi) &= \frac{p_0 z_0}{p_0 + p_z} + \frac{1}{(p_0 + p_z)^2} \int_{-\infty}^{\xi} \left[ p_x q A_x - \frac{q^2 A_x^2}{2} \right] d\xi' + \frac{p_z \xi}{p_0 + p_z},
\end{aligned} \tag{A4}$$

where for convenience of expression the notation  $p_0 = \sqrt{m_e^2 c^2 + \vec{p} \cdot \vec{p}} = \gamma m_e c$  has been introduced. Before the arrival of the laser pulse, the integrals are negligible and  $ct \rightarrow p_0(\xi - z_0)/(p_0 + p_z)$ . Thus

$$\begin{aligned}
x(\xi(t)) &\rightarrow x_0 + \frac{p_x}{p_0} ct = x_0 + \beta_x ct, \\
y(\xi(t)) &\rightarrow y_0 + \frac{p_y}{p_0} ct = y_0 + \beta_y ct, \\
z(\xi(t)) &\rightarrow z_0 + \frac{p_z}{p_0} ct = z_0 + \beta_z ct,
\end{aligned} \tag{A5}$$

consistent with the definition of the initial 4-momentum. Consequently, one can interpret the constant vector  $(x_0, y_0, z_0)$  as the offset the electron would have at the time the  $\xi = 0$  point in the laser pulse crosses the interaction point (at the origin of the coordinate system) if there were no electromagnetic force acting on the electron. If a particle is located at  $z = z_0$  when  $t = 0$ , it takes a time  $\Delta t = -z_0/(1 + \beta_z)c$  to propagate to the condition  $\xi = 0$ . The offsets proportional to  $-z_0/(1 + \beta_z)$  in the equations for each of the coordinates clearly compensate for this time offset when expressing the orbits in terms of  $\xi$ . In the case that the electron's transverse location does not change much when the laser pulse is traversed, the transverse integration constants  $x_0$  and  $y_0$  can be used to capture any transverse dependence of the laser

vector potential. For our solutions in this paper, these effects are included using a simple model.

## APPENDIX B: CONSISTENCY CHECK AND SOLUTION FOR GENERAL SCATTERING GEOMETRY

To verify our result for the lab frame scattered spectral energy density is correct in detail, we carry out a second calculation in a primed “rest” frame of the electron before the arrival of the laser pulse with the large longitudinal velocity subtracted out. Then the transverse velocity is very small, and the transformation formulas for the angles can proceed as before. In the primed frame

$$\begin{aligned}
ct'(\xi') &= -z_0 + \int_{-\infty}^{\xi'} \left[ \frac{e}{m_e c} \beta'_x \frac{A'_x}{\gamma'} + \frac{e^2}{2m_e^2 c^2} \frac{A_x'^2}{\gamma'^2} \right] d\xi'' + \xi', \\
x'(\xi') &= x_0 + \int_{-\infty}^{\xi'} \frac{e A'_x}{m_e c \gamma'} d\xi'' + \beta'_x \xi', \\
y'(\xi') &= y_0 + \beta'_y \xi', \\
z'(\xi') &= z_0 - \int_{-\infty}^{\xi'} \left[ \frac{e}{m_e c} \beta'_x \frac{A'_x}{\gamma'} + \frac{e^2}{2m_e^2 c^2} \frac{A_x'^2}{\gamma'^2} \right] d\xi''.
\end{aligned} \tag{B1}$$

For the electrodynamic part, by inspection the previous expressions can be used by simply setting  $\beta_z = 0$ . So

$$\begin{aligned}
\frac{dE'_{\perp}}{d\omega'' d\Omega'} &= \frac{e^2 \omega'^2}{16\pi^3 \epsilon_0 c^3} \left| D'_1 \sin \varphi - \beta'_x \frac{[\beta'_x(1 + \cos \theta') - \sin \theta' \cos \varphi'] D'_1 + (1 + \cos \theta') D'_2}{(1 - \beta'_x \sin \theta' \cos \varphi' - \beta'_y \sin \theta' \sin \varphi')} \sin \varphi' \right. \\
&\quad \left. + \beta'_y \frac{[\beta'_x(1 + \cos \theta') - \sin \theta' \cos \varphi'] D'_1 + (1 + \cos \theta') D'_2}{(1 - \beta'_x \sin \theta' \cos \varphi' - \beta'_y \sin \theta' \sin \varphi')} \cos \varphi' \right|^2
\end{aligned} \tag{B2}$$

and

$$\begin{aligned}
\frac{dE'_{\parallel}}{d\omega''d\Omega'} &= \frac{e^2\omega'^2}{16\pi^3\epsilon_0c^3} \left| D'_1 \frac{\cos\theta'\cos\varphi'}{1-\beta'_x\sin\theta'\cos\varphi'-\beta'_y\sin\theta'\sin\varphi'} - D'_1 \frac{(\beta'_x\sin\theta'\cos\varphi'+\beta'_y\sin\theta'\sin\varphi')\cos\theta'\cos\varphi'}{1-\beta'_x\sin\theta'\cos\varphi'-\beta'_y\sin\theta'\sin\varphi'} \right. \\
&\quad - \beta'_x \frac{[\beta'_x(1+\cos\theta')-\sin\theta'\cos\varphi']D'_1 + (1+\cos\theta')D'_2}{1-\beta'_x\sin\theta'\cos\varphi'-\beta'_y\sin\theta'\sin\varphi'} \cos\theta'\cos\varphi' \\
&\quad - \beta'_y \frac{[\beta'_x(1+\cos\theta')-\sin\theta'\cos\varphi']D'_1 + (1+\cos\theta')D'_2}{1-\beta'_x\sin\theta'\cos\varphi'-\beta'_y\sin\theta'\sin\varphi'} \cos\theta'\sin\varphi' \\
&\quad + D'_2 \sin\theta' \frac{1}{1-\beta'_x\sin\theta'\cos\varphi'-\beta'_y\sin\theta'\sin\varphi'} \\
&\quad \left. - D'_2 \sin\theta' \frac{(\beta'_x\sin\theta'\cos\varphi'+\beta'_y\sin\theta'\sin\varphi')}{1-\beta'_x\sin\theta'\cos\varphi'-\beta'_y\sin\theta'\sin\varphi'} + \beta'_xD'_1 \sin\theta' \right|^2, \tag{B3}
\end{aligned}$$

where

$$\begin{aligned}
D'_1(\omega''; \theta, \varphi) &= \frac{1}{\gamma'} \int \frac{eA'_x(\xi')}{m_e c} e^{i\varphi'} d\xi', \\
D'_2(\omega''; \theta, \varphi) &= \frac{1}{\gamma'^2} \int \frac{e^2 A_x'^2(\xi')}{2m_e^2 c^2} e^{i\varphi'} d\xi', \\
\varphi'(\xi') &= \frac{\omega''}{c} \left( \xi'(1-\beta'_x\sin\theta'\cos\varphi'-\beta'_y\sin\theta'\sin\varphi') \right. \\
&\quad \left. + [\beta'_x(1+\cos\theta')-\sin\theta'\cos\varphi'] \int_{-\infty}^{\xi'} \frac{eA'_x(\xi'')}{\gamma' m_e c} d\xi'' + (1+\cos\theta') \int_{-\infty}^{\xi'} \frac{e^2 A_x'^2(\xi'')}{\gamma'^2 2m_e^2 c^2} d\xi'' \right), \tag{B4}
\end{aligned}$$

and where  $\omega''$  is the scattered frequency in the primed frame, reserving  $\omega'$  to denote the scattered frequency in the lab frame. Note that  $\gamma' = 1/\sqrt{1-\beta_x'^2-\beta_y'^2}$  is the relativistic gamma computed with the small transverse velocities and is close to 1. As above, put all terms over a common denominator. One obtains

$$\begin{aligned}
\frac{dE'_{\perp}}{d\omega''d\Omega'} &= \frac{e^2\omega'^2}{16\pi^3\epsilon_0c^3} \left| \frac{D'_1[\sin\varphi'-\beta'_y\sin\theta']}{1-\beta'_x\sin\theta'\cos\varphi'-\beta'_y\sin\theta'\sin\varphi'} - \beta'_x \frac{[\beta'_x(1+\cos\theta')]D'_1 + (1+\cos\theta')D'_2}{1-\beta'_x\sin\theta'\cos\varphi'-\beta'_y\sin\theta'\sin\varphi'} \sin\varphi' \right. \\
&\quad \left. + \beta'_y \frac{[\beta'_x(1+\cos\theta')]D'_1 + (1+\cos\theta')D'_2}{1-\beta'_x\sin\theta'\cos\varphi'-\beta'_y\sin\theta'\sin\varphi'} \cos\varphi' \right|^2 \tag{B5}
\end{aligned}$$

and

$$\begin{aligned}
\frac{dE'_{\parallel}}{d\omega''d\Omega'} &= \frac{e^2\omega'^2}{16\pi^3\epsilon_0c^3} \left| \frac{D'_1\cos\theta'\cos\varphi'}{1-\beta'_x\sin\theta'\cos\varphi'-\beta'_y\sin\theta'\sin\varphi'} - \beta'_x \frac{\beta'_x(1+\cos\theta')D'_1 + (1+\cos\theta')D'_2}{1-\beta'_x\sin\theta'\cos\varphi'-\beta'_y\sin\theta'\sin\varphi'} \cos\varphi' \right. \\
&\quad - \beta'_y \frac{\beta'_x(1+\cos\theta')D'_1 + (1+\cos\theta')D'_2}{1-\beta'_x\sin\theta'\cos\varphi'-\beta'_y\sin\theta'\sin\varphi'} \sin\varphi' + \frac{D'_2}{1-\beta'_x\sin\theta'\cos\varphi'-\beta'_y\sin\theta'\sin\varphi'} \sin\theta' k_0 \\
&\quad \left. + \frac{\beta'_xD'_1}{1-\beta'_x\sin\theta'\cos\varphi'-\beta'_y\sin\theta'\sin\varphi'} \sin\theta' \right|^2. \tag{B6}
\end{aligned}$$

We now perform a consistency check. If we Lorentz transform with the electron longitudinal velocity back to the laboratory frame, we should recover the lab frame result. Defining  $\gamma_{\beta_z} = 1/\sqrt{1-\beta_z^2}$ , the 4-velocity transforms as

$$\begin{aligned}
\gamma' &= \gamma_{\beta_z}(\gamma - \beta_z(\beta_z\gamma)) \\
\gamma'\beta'_x &= \gamma\beta_x \\
\gamma'\beta'_y &= \gamma\beta_y \\
\gamma'\beta'_z &= \gamma_{\beta_z}(\beta_z\gamma - \beta_z\gamma) = 0, \tag{B7}
\end{aligned}$$

which implies  $\gamma'\gamma_{\beta_z} = \gamma$ . Now the scattering angles transform as

$$\begin{aligned}\sin \theta' &= \frac{\sin \theta}{\gamma_{\beta_z}(1 - \beta_z \cos \theta)} \\ \cos \theta' &= \frac{\cos \theta - \beta_z}{1 - \beta_z \cos \theta} \\ \varphi' &= \varphi\end{aligned}\tag{B8}$$

and so

$$\begin{aligned}1 - \beta'_x \sin \theta' \cos \varphi' - \beta'_y \sin \theta' \sin \varphi' &= 1 - \frac{\gamma'(\beta'_x \sin \theta' \cos \varphi' + \beta'_y \sin \theta' \sin \varphi')}{\gamma'} \\ &= 1 - \frac{\gamma\beta_x \sin \theta' \cos \varphi' + \gamma\beta_y \sin \theta' \sin \varphi'}{\gamma'} \\ &= 1 - \frac{\gamma\beta_x \sin \theta \cos \varphi + \gamma\beta_y \sin \theta \sin \varphi}{\gamma'\gamma_{\beta_z}(1 - \beta_z \cos \theta)} \\ &= \frac{1 - \beta_z \cos \theta - \beta_x \sin \theta \cos \varphi - \beta_y \sin \theta \sin \varphi}{1 - \beta_z \cos \theta}.\end{aligned}\tag{B9}$$

Some other needed transformation rules are  $\omega'' = \gamma_{\beta_z}(1 - \beta_z \cos \theta)\omega'$ ,

$$\begin{aligned}1 + \cos \theta' &= 1 + \frac{\cos \theta - \beta_z}{1 - \beta_z \cos \theta} = \frac{(1 - \beta_z)(1 + \cos \theta)}{1 - \beta_z \cos \theta} = \frac{1 + \cos \theta}{(1 + \beta_z)\gamma_{\beta_z}^2(1 - \beta_z \cos \theta)}, \\ \beta'_x &= \frac{\gamma\beta_x}{\gamma'}, \quad \text{and} \quad \beta'_y = \frac{\gamma\beta_y}{\gamma'}.\end{aligned}\tag{B10}$$

To get the transformation of the integrating phase note by the Lorentz transformation

$$\xi' = ct' + z' = \gamma_{\beta_z}(ct - \beta_z z) + \gamma_{\beta_z}(-\beta_z ct + z) = \gamma_{\beta_z}(ct + z)(1 - \beta_z) = \frac{ct + z}{\gamma_{\beta_z}(1 + \beta_z)} = \frac{\xi}{\gamma_{\beta_z}(1 + \beta_z)}.\tag{B11}$$

Also the vector potential, as it is purely transverse to the transformation, satisfies

$$A'(\xi') = A(\xi) = A(\xi'\gamma_{\beta_z}(1 + \beta_z)).\tag{B12}$$

So the integrals satisfy

$$\begin{aligned}\int_{-\infty}^{\xi'} A'(\xi'') d\xi'' &= \int_{-\infty}^{\xi'} A(\xi''\gamma_{\beta_z}(1 + \beta_z)) d\xi'' \\ &= \frac{1}{\gamma_{\beta_z}(1 + \beta_z)} \int_{-\infty}^{\xi'\gamma_{\beta_z}(1 + \beta_z)} A(\xi''') d\xi''' \\ &= \frac{1}{\gamma_{\beta_z}(1 + \beta_z)} \int_{-\infty}^{\xi} A(\xi'') d\xi'',\end{aligned}\tag{B13}$$

and similarly

$$\int_{-\infty}^{\xi'} A'^2(\xi'')/2 d\xi'' = \frac{1}{\gamma_{\beta_z}(1 + \beta_z)} \int_{-\infty}^{\xi} A^2(\xi'')/2 d\xi''.\tag{B14}$$

So indeed

$$\begin{aligned}
\varphi'(\xi') &\rightarrow \frac{\omega' \gamma_{\beta_z} (1 - \beta_z \cos \theta)}{c} \left( \frac{\xi}{\gamma_{\beta_z} (1 + \beta_z)} \frac{1 - \beta_x \sin \theta \cos \varphi - \beta_y \sin \theta \sin \varphi - \beta_z \cos \theta}{1 - \beta_z \cos \theta} \right. \\
&+ \left[ \frac{\gamma_{\beta_x} \frac{(1 + \cos \theta)}{\gamma' \gamma_{\beta_z}^2 (1 - \beta_z \cos \theta)(1 + \beta_z)}}{-\frac{\sin \theta}{\gamma_{\beta_z} (1 - \beta_z \cos \theta)} \cos \varphi} \right] \frac{1}{\gamma_{\beta_z} (1 + \beta_z)} \frac{1}{\gamma'} \int_{-\infty}^{\xi} \frac{eA(\xi'')}{m_e c} d\xi'' \\
&+ \left. \frac{(1 + \cos \theta)}{\gamma_{\beta_z}^2 (1 - \beta_z \cos \theta)(1 + \beta_z)} \frac{1}{\gamma'^2} \frac{1}{\gamma_{\beta_z} (1 + \beta_z)} \int_{-\infty}^{\xi} \frac{e^2 A_x^2(\xi'')}{2m_e^2 c^2} d\xi'' \right) \\
&= \Phi(\xi),
\end{aligned} \tag{B15}$$

and for the distribution functions

$$\begin{aligned}
D'_1 \cos \theta' \cos \varphi' &\rightarrow D_1 \frac{\cos \theta - \beta_z}{1 - \beta_z \cos \theta} \cos \varphi, \\
D'_2 \sin \theta' &\rightarrow \gamma_{\beta_z} (1 + \beta_z) D_2 \frac{\sin \theta}{\gamma_{\beta_z} (1 - \beta_z \cos \theta)}, \\
\beta'_y \frac{[\beta'_x (1 + \cos \theta') - \sin \theta' \cos \varphi'] D'_1 + (1 + \cos \theta') D'_2}{(1 - \beta'_x \sin \theta' \cos \varphi' - \beta'_y \sin \theta' \cos \varphi')} &\rightarrow \beta_y \frac{[\beta_x (1 + \cos \theta) / (1 + \beta_z) - \sin \theta \cos \varphi] D_1 + (1 + \cos \theta) D_2}{1 - \beta_x \sin \theta \cos \varphi - \beta_y \sin \theta \cos \varphi - \beta_z \cos \theta}, \\
\beta'_x D'_1 \sin \theta' &\rightarrow \frac{\gamma_{\beta_x}}{\gamma'} D_1 \frac{\sin \theta}{\gamma_{\beta_z} (1 - \beta_z \cos \theta)} = \beta_x D_1 \frac{\sin \theta}{(1 - \beta_z \cos \theta)}.
\end{aligned} \tag{B16}$$

The transformed distribution is identical to the one calculated in the lab frame to begin with.

Likewise, the expressions in the paper can be used to find the polarization vector in the beam frame as

### 1. General geometry

From Ref. [2], we have the general Lorentz transformation rule for electromagnetic radiation from the lab frame to a frame moving with relativistic velocity  $(\beta_x, \beta_y, \beta_z)$ . The unit wave vector in the moving frame is

$$\hat{k}_b = \frac{1}{\gamma(1 - \vec{\beta} \cdot \hat{k})} \left[ -\gamma \vec{\beta} + \hat{k} + \frac{\gamma - 1}{\beta^2} (\vec{\beta} \cdot \hat{k}) \vec{\beta} \right]. \tag{B17}$$

$$\epsilon_b = \epsilon + \frac{(\vec{\beta} \cdot \epsilon)}{(1 - \vec{\beta} \cdot \hat{k})} \left[ -\gamma \vec{\beta} + \hat{k} + \frac{\gamma - 1}{\beta^2} \vec{\beta} \right]. \tag{B18}$$

With vector potential  $A(\xi) \vec{\epsilon}$  and now  $\xi = (ct - \hat{k} \cdot \vec{x})$  with  $\vec{\epsilon} \cdot \hat{k} = 0$ , the general action solving the Hamilton-Jacobi equation contains

$$F(\xi) = \int_{-\infty}^{\xi} \left[ \frac{\vec{p} \cdot \vec{\epsilon} [qA(\xi')]}{\sqrt{m_e^2 c^2 + \vec{p} \cdot \vec{p} - \vec{p} \cdot \hat{k}}} - \frac{q^2 A^2(\xi')/2}{\sqrt{m_e^2 c^2 + \vec{p} \cdot \vec{p} - \vec{p} \cdot \hat{k}}} \right] d\xi'. \tag{B19}$$

After a calculation entirely analogous to that shown in Appendix A, the solution to the equations of motion is found to be

$$\begin{aligned}
ct(\xi) &= \frac{(\hat{k} \cdot \vec{x}_0) \sqrt{m_e^2 c^2 + \vec{p} \cdot \vec{p}}}{\sqrt{m_e^2 c^2 + \vec{p} \cdot \vec{p} - \vec{p} \cdot \hat{k}}} - \frac{\vec{\epsilon} \cdot \vec{p}}{(\sqrt{m_e^2 c^2 + \vec{p} \cdot \vec{p} - \vec{p} \cdot \hat{k}})^2} \int_{-\infty}^{\xi} qA d\xi' \\
&+ \frac{1}{(\sqrt{m_e^2 c^2 + \vec{p} \cdot \vec{p} - \vec{p} \cdot \hat{k}})^2} \int_{-\infty}^{\xi} \frac{q^2 A^2}{2} d\xi' + \frac{\sqrt{m_e^2 c^2 + \vec{p} \cdot \vec{p}}}{\sqrt{m_e^2 c^2 + \vec{p} \cdot \vec{p} - \vec{p} \cdot \hat{k}}} \xi,
\end{aligned}$$

$$\begin{aligned}
x(\xi) &= x_0 + \frac{(\hat{k} \cdot \vec{x}_0)p_x}{\sqrt{m_e^2 c^2 + \vec{p} \cdot \vec{p} - \vec{p} \cdot \hat{k}}} - \frac{(\vec{\epsilon} \cdot \vec{p})\hat{k}_x}{(\sqrt{m_e^2 c^2 + \vec{p} \cdot \vec{p} - \vec{p} \cdot \hat{k}})^2} \int_{-\infty}^{\xi} qA d\xi' - \frac{\epsilon_x}{\sqrt{m_e^2 c^2 + \vec{p} \cdot \vec{p} - \vec{p} \cdot \hat{k}}} \int_{-\infty}^{\xi} qA d\xi' \\
&\quad + \frac{\hat{k}_x}{(\sqrt{m_e^2 c^2 + \vec{p} \cdot \vec{p} - \vec{p} \cdot \hat{k}})^2} \int_{-\infty}^{\xi} \frac{q^2 A^2}{2} d\xi' + \frac{p_x}{\sqrt{m_e^2 c^2 + \vec{p} \cdot \vec{p} - \vec{p} \cdot \hat{k}}} \xi, \\
y(\xi) &= y_0 + \frac{(\hat{k} \cdot \vec{x}_0)p_y}{\sqrt{m_e^2 c^2 + \vec{p} \cdot \vec{p} - \vec{p} \cdot \hat{k}}} - \frac{(\vec{\epsilon} \cdot \vec{p})\hat{k}_y}{(\sqrt{m_e^2 c^2 + \vec{p} \cdot \vec{p} - \vec{p} \cdot \hat{k}})^2} \int_{-\infty}^{\xi} qA d\xi' - \frac{\epsilon_y}{\sqrt{m_e^2 c^2 + \vec{p} \cdot \vec{p} - \vec{p} \cdot \hat{k}}} \int_{-\infty}^{\xi} qA d\xi' \\
&\quad + \frac{\hat{k}_y}{(\sqrt{m_e^2 c^2 + \vec{p} \cdot \vec{p} - \vec{p} \cdot \hat{k}})^2} \int_{-\infty}^{\xi} \frac{q^2 A^2}{2} d\xi' + \frac{p_y}{\sqrt{m_e^2 c^2 + \vec{p} \cdot \vec{p} - \vec{p} \cdot \hat{k}}} \xi, \\
z(\xi) &= z_0 + \frac{(\hat{k} \cdot \vec{x}_0)p_z}{\sqrt{m_e^2 c^2 + \vec{p} \cdot \vec{p} - \vec{p} \cdot \hat{k}}} - \frac{(\vec{\epsilon} \cdot \vec{p})\hat{k}_z}{(\sqrt{m_e^2 c^2 + \vec{p} \cdot \vec{p} - \vec{p} \cdot \hat{k}})^2} \int_{-\infty}^{\xi} qA d\xi' - \frac{\epsilon_z}{\sqrt{m_e^2 c^2 + \vec{p} \cdot \vec{p} - \vec{p} \cdot \hat{k}}} \int_{-\infty}^{\xi} qA d\xi' \\
&\quad + \frac{\hat{k}_z}{(\sqrt{m_e^2 c^2 + \vec{p} \cdot \vec{p} - \vec{p} \cdot \hat{k}})^2} \int_{-\infty}^{\xi} \frac{q^2 A^2}{2} d\xi' + \frac{p_z}{\sqrt{m_e^2 c^2 + \vec{p} \cdot \vec{p} - \vec{p} \cdot \hat{k}}} \xi. \tag{B20}
\end{aligned}$$

The electrodynamic calculation proceeds as before with result

$$\begin{aligned}
\frac{d^2 E'_{\perp}}{d\omega' d\Omega} &= \frac{e^2 \omega'^2}{16\pi^3 \epsilon_0 c^3} \left| D_1(\vec{\epsilon} \cdot \vec{\epsilon}'_{\perp}) + D_1 \frac{\vec{p} \cdot \vec{\epsilon}}{\sqrt{m_e^2 c^2 + \vec{p} \cdot \vec{p} - \vec{p} \cdot \hat{k}}} (\hat{k} \cdot \vec{\epsilon}'_{\perp}) - D_2(\hat{k} \cdot \vec{\epsilon}'_{\perp}) \right. \\
&\quad \left. - \frac{[(\vec{p} \cdot \vec{\epsilon})(1 - \hat{k}' \cdot \hat{k}) / (\sqrt{m_e^2 c^2 + \vec{p} \cdot \vec{p} - \vec{p} \cdot \hat{k}}) - (\hat{k}' \cdot \vec{\epsilon})] D_1 - (1 - \hat{k}' \cdot \hat{k}) D_2}{\sqrt{m_e^2 c^2 + \vec{p} \cdot \vec{p} - \vec{p} \cdot \hat{k}}} \vec{p} \cdot \vec{\epsilon}'_{\perp} \right|^2 \tag{B21}
\end{aligned}$$

and

$$\begin{aligned}
\frac{d^2 E'_{\parallel}}{d\omega' d\Omega} &= \frac{e^2 \omega'^2}{16\pi^3 \epsilon_0 c^3} \left| D_1(\vec{\epsilon} \cdot \vec{\epsilon}'_{\parallel}) + D_1 \frac{\vec{p} \cdot \vec{\epsilon}}{\sqrt{m_e^2 c^2 + \vec{p} \cdot \vec{p} - \vec{p} \cdot \hat{k}}} (\hat{k} \cdot \vec{\epsilon}'_{\parallel}) - D_2(\hat{k} \cdot \vec{\epsilon}'_{\parallel}) \right. \\
&\quad \left. - \frac{[(\vec{p} \cdot \vec{\epsilon})(1 - \hat{k}' \cdot \hat{k}) / (\sqrt{m_e^2 c^2 + \vec{p} \cdot \vec{p} - \vec{p} \cdot \hat{k}}) - (\hat{k}' \cdot \vec{\epsilon})] D_1 - (1 - \hat{k}' \cdot \hat{k}) D_2}{\sqrt{m_e^2 c^2 + \vec{p} \cdot \vec{p} - \vec{p} \cdot \hat{k}}} \vec{p} \cdot \vec{\epsilon}'_{\parallel} \right|^2, \tag{B22}
\end{aligned}$$

where

$$\begin{aligned}
D_1(\omega'; \theta, \varphi) &= \frac{1}{\sqrt{m_e^2 c^2 + \vec{p} \cdot \vec{p} - \vec{p} \cdot \hat{k}}} \int qA(\xi') e^{i\Phi(\xi')} d\xi', \\
D_2(\omega'; \theta, \varphi) &= \frac{1}{(\sqrt{m_e^2 c^2 + \vec{p} \cdot \vec{p} - \vec{p} \cdot \hat{k}})^2} \int \frac{q^2 A^2(\xi')}{2} e^{i\Phi(\xi')} d\xi', \\
\Phi(\xi') &= \frac{\omega'}{c} \left( \xi' \frac{\sqrt{m_e^2 c^2 + \vec{p} \cdot \vec{p} - \vec{p} \cdot \hat{k}'}}{\sqrt{m_e^2 c^2 + \vec{p} \cdot \vec{p} - \vec{p} \cdot \hat{k}}} - \left[ \frac{\vec{p} \cdot \vec{\epsilon}}{\sqrt{m_e^2 c^2 + \vec{p} \cdot \vec{p} - \vec{p} \cdot \hat{k}}} (1 - \hat{k}' \cdot \hat{k}) - \hat{k}' \cdot \vec{\epsilon} \right] \right. \\
&\quad \left. \times \int_{-\infty}^{\xi'} \frac{qA(\xi'')}{\sqrt{m_e^2 c^2 + \vec{p} \cdot \vec{p} - \vec{p} \cdot \hat{k}}} d\xi'' + (1 - \hat{k}' \cdot \hat{k}) \int_{-\infty}^{\xi'} \frac{q^2 A^2(\xi'')}{2(\sqrt{m_e^2 c^2 + \vec{p} \cdot \vec{p} - \vec{p} \cdot \hat{k}})^2} d\xi'' \right). \tag{B23}
\end{aligned}$$

For the given scattering variables the spectra are

$$\begin{aligned}
\frac{d^2 E'_{\perp}}{d\omega' d\Omega} &= \frac{e^2 \omega'^2}{16\pi^3 \epsilon_0 c^3} \left| D_1(\vec{\epsilon} \cdot \vec{\epsilon}'_{\perp}) + D_1 \frac{\vec{p} \cdot \vec{\epsilon}}{\sqrt{m_e^2 c^2 + \vec{p} \cdot \vec{p} - \vec{p} \cdot \hat{k}}} (\hat{k} \cdot \vec{\epsilon}'_{\perp}) - D_2(\hat{k} \cdot \vec{\epsilon}'_{\perp}) \right. \\
&\quad + \beta_x \frac{[(\vec{p} \cdot \vec{\epsilon})(1 - \hat{k}' \cdot \hat{k}) / (\sqrt{m_e^2 c^2 + \vec{p} \cdot \vec{p} - \vec{p} \cdot \hat{k}}) - (\hat{k}' \cdot \vec{\epsilon})] D_1 - (1 - \hat{k}' \cdot \hat{k}) D_2}{1 - \beta_x \cos \phi \sin \theta - \beta_y \sin \phi \sin \theta - \beta_z \cos \theta} \sin \phi \\
&\quad \left. - \beta_y \frac{[(\vec{p} \cdot \vec{\epsilon})(1 - \hat{k}' \cdot \hat{k}) / (\sqrt{m_e^2 c^2 + \vec{p} \cdot \vec{p} - \vec{p} \cdot \hat{k}}) - (\hat{k}' \cdot \vec{\epsilon})] D_1 - (1 - \hat{k}' \cdot \hat{k}) D_2}{1 - \beta_x \cos \phi \sin \theta - \beta_y \sin \phi \sin \theta - \beta_z \cos \theta} \cos \phi \right|^2 \tag{B24}
\end{aligned}$$

and

$$\begin{aligned}
\frac{d^2 E'_{\parallel}}{d\omega' d\Omega} = & \frac{e^2 \omega'^2}{16\pi^3 \epsilon_0 c^3} \left| D_1(\vec{\epsilon} \cdot \vec{\epsilon}'_{\parallel}) + D_1 \frac{\vec{p} \cdot \vec{\epsilon}}{\sqrt{m_e^2 c^2 + \vec{p} \cdot \vec{p} - \vec{p} \cdot \hat{k}}} (\hat{k} \cdot \vec{\epsilon}'_{\parallel}) - D_2(\hat{k} \cdot \vec{\epsilon}'_{\parallel}) \right. \\
& - \beta_x \frac{[(\vec{p} \cdot \vec{\epsilon})(1 - \hat{k}' \cdot \hat{k}) / (\sqrt{m_e^2 c^2 + \vec{p} \cdot \vec{p} - \vec{p} \cdot \hat{k}}) - (\hat{k}' \cdot \vec{\epsilon})] D_1 - (1 - \hat{k}' \cdot \hat{k}) D_2}{1 - \beta_x \cos \phi \sin \theta - \beta_y \sin \phi \sin \theta - \beta_z \cos \theta} \cos \phi \cos \theta \\
& - \beta_y \frac{[(\vec{p} \cdot \vec{\epsilon})(1 - \hat{k}' \cdot \hat{k}) / (\sqrt{m_e^2 c^2 + \vec{p} \cdot \vec{p} - \vec{p} \cdot \hat{k}}) - (\hat{k}' \cdot \vec{\epsilon})] D_1 - (1 - \hat{k}' \cdot \hat{k}) D_2}{1 - \beta_x \cos \phi \sin \theta - \beta_y \sin \phi \sin \theta - \beta_z \cos \theta} \sin \phi \cos \theta \\
& \left. + \beta_z \frac{[(\vec{p} \cdot \vec{\epsilon})(1 - \hat{k}' \cdot \hat{k}) / (\sqrt{m_e^2 c^2 + \vec{p} \cdot \vec{p} - \vec{p} \cdot \hat{k}}) - (\hat{k}' \cdot \vec{\epsilon})] D_1 - (1 - \hat{k}' \cdot \hat{k}) D_2}{1 - \beta_x \cos \phi \sin \theta - \beta_y \sin \phi \sin \theta - \beta_z \cos \theta} \sin \theta \right|^2. \quad (B25)
\end{aligned}$$

It should be noted that in the formulas for the spectra, the perpendicular polarization is defined to be in the direction  $\hat{z} \times \vec{k}'$  and the parallel polarization in the direction  $(\hat{z} \times \vec{k}') \times \vec{k}'$ . Thus it is assumed that the electron beam average velocity is in the  $\hat{z}$  direction, even if the individual electron orbits are not exactly in this direction.

During these derivations it is important to apply the more general integral conversion prescription

$$\int e^{i\Phi} d\xi \rightarrow \frac{[(\vec{p} \cdot \vec{\epsilon})(1 - \hat{k}' \cdot \hat{k}) - (\sqrt{m_e^2 c^2 + \vec{p} \cdot \vec{p} - \vec{p} \cdot \hat{k}})(\hat{k}' \cdot \vec{\epsilon})] D_1 - (\sqrt{m_e^2 c^2 + \vec{p} \cdot \vec{p} - \vec{p} \cdot \hat{k}})(1 - \hat{k}' \cdot \hat{k}) D_2}{\sqrt{m_e^2 c^2 + \vec{p} \cdot \vec{p} - \vec{p} \cdot \hat{k}}}. \quad (B26)$$

- 
- |   |  |
|---|--|
| <p>[1] J. Huang, B. Günther, K. Achterhold, Y. Cui, B. Gleich, M. Dierolf, and F. Pfeiffer, <i>Sci. Rep.</i> <b>10</b>, 8772 (2020).</p> <p>[2] G. Krafft, E. Johnson, K. Deitrick, B. Terzić, R. Kelmar, T. Hodges, W. Melnitchouk, and J. Delayen, <i>Phys. Rev. Accel. Beams</i> <b>19</b>, 121302 (2016).</p> <p>[3] K. Deitrick, Ph.D. thesis, Old Dominion University, 2017.</p> <p>[4] J. Luiten, <i>Smart*Light: a Dutch Table-Top Synchrotron Light Source</i> (T.U. Eindhoven, Eindhoven, Netherlands, 2020).</p> <p>[5] Lyncean Technologies Inc. <a href="https://lynceantech.com/products/">https://lynceantech.com/products/</a>. Accessed: 2021-12-06.</p> <p>[6] R. Coisson, <i>Phys. Rev. A</i> <b>20</b>, 524 (1979).</p> <p>[7] P. Chen, G. Horton-Smith, T. Ohgaki, A. Weidemann, and K. Yokoya, <i>Nucl. Instrum. Methods Phys. Res., Sect. A</i> <b>355</b>, 107 (1995).</p> <p>[8] B. Terzić, A. Brown, I. Drebot, T. Hagerman, E. Johnson, G. Krafft, C. Maroli, V. Petrillo, and M. Ruijter, <i>Europhys. Lett.</i> <b>126</b>, 12003 (2019).</p> <p>[9] G. Krafft, <i>Phys. Rev. Lett.</i> <b>92</b>, 204802 (2004).</p> <p>[10] I. Ghebregziabher, B. Shadwick, and D. Umstadter, <i>Phys. Rev. ST Accel. Beams</i> <b>16</b>, 030705 (2013).</p> <p>[11] B. Terzić, K. Deitrick, A. Hofler, and G. Krafft, <i>Phys. Rev. Lett.</i> <b>112</b>, 074801 (2014).</p> <p>[12] C. Maroli, V. Petrillo, I. Drebot, L. Serafini, B. Terzić, and G. Krafft, <i>J. Appl. Phys.</i> <b>124</b>, 063105 (2018).</p> <p>[13] K. Deitrick, G. H. Hoffstaetter, C. Franck, B. D. Muratori, P. H. Williams, G. A. Krafft, B. Terzić, J. Crone, and H. Owen, <i>Phys. Rev. Accel. Beams</i> <b>24</b>, 050701 (2021).</p> <p>[14] X. Artru, <i>Phys. Rev. Accel. Beams</i>, <b>22</b>, 050705 (2019).</p> <p>[15] T. Wistisen, <i>Phys. Rev. D</i> <b>90</b>, 125008 (2014).</p> <p>[16] A. Di Piazza, <i>Phys. Rev. Lett.</i> <b>113</b>, 040402 (2014).</p> <p>[17] A. Di Piazza, <i>Phys. Rev. D</i> <b>103</b>, 076011 (2021).</p> <p>[18] I. Goldman, <i>Phys. Lett.</i> <b>8</b>, 103 (1964).</p> | <p>[19] F. Vélez, J. Kamiński, and K. Krajewska, <i>Atoms</i> <b>7</b>, 34 (2019).</p> <p>[20] K. Krajewska and J. Kamiński, <i>Phys. Rev. A</i> <b>85</b>, 062102 (2012).</p> <p>[21] D. Seipt and B. Kämpfer, <i>Phys. Rev. A</i> <b>83</b>, 022101 (2011).</p> <p>[22] D. Seipt, A. Surzhykov, S. Fritzsche, and B. Kämpfer, <i>New J. Phys.</i> <b>18</b>, 023044 (2016).</p> <p>[23] F. Mackenroth and A. Di Piazza, <i>Phys. Rev. A</i> <b>83</b>, 032106 (2011).</p> <p>[24] M. Boca and V. Florescu, <i>Phys. Rev. A</i> <b>80</b>, 053403 (2009).</p> <p>[25] M. Boca, <i>Open Physics</i> <b>11</b>, 1123 (2013).</p> <p>[26] V. Kharin, D. Seipt, and S. Rykovanov, <i>Phys. Rev. Lett.</i> <b>120</b>, 044802 (2018).</p> <p>[27] A. Angioi, F. Mackenroth, and A. Di Piazza, <i>Phys. Rev. A</i> <b>93</b>, 052102 (2016).</p> <p>[28] C. Harvey, A. Gonoskov, M. Marklund, and E. Wallin, <i>Phys. Rev. A</i> <b>93</b>, 022112 (2016).</p> <p>[29] G. Krafft and G. Priebe, <i>Rev. Accel. Sci. Technol.</i> <b>03</b>, 147 (2010).</p> <p>[30] P. Duke, <i>Synchrotron Radiation: Production and Properties</i> (Oxford Science, New York, 2000).</p> <p>[31] J. Clarke, <i>The Science and Technology of Undulators and Wigglers</i> (Oxford Series on Synchrotron Radiation, New York, 2004).</p> <p>[32] J. Jackson, <i>Classical Electrodynamics</i> 3rd ed. (John Wiley &amp; Sons, New York, 1999).</p> <p>[33] L. Landau and E. Lifshitz, <i>The Classical Theory of Fields: Volume 2 Course of Theoretical Physics</i>, 3rd ed. (Butterworth-Heinemann, Oxford, 1976).</p> <p>[34] A. Di Piazza, <i>Lett. Math. Phys.</i> <b>83</b>, 305 (2008).</p> <p>[35] J. Krämer <i>et al.</i>, <i>Sci. Rep.</i> <b>8</b>, 1398 (2018).</p> <p>[36] N. Ranjan, B. Terzić, G. Krafft, V. Petrillo, I. Drebot, and L. Serafini, <i>Phys. Rev. Accel. Beams</i> <b>21</b>, 030701 (2018).</p> <p>[37] L. Landau and E. Lifshitz, <i>Mechanics: Volume 1 Course of Theoretical Physics</i>, 3rd ed. (Butterworth-Heinemann, Oxford, 1976).</p> |
|---|--|